α-catenin middle- and actin-binding domain unfolding mutants differentially impact epithelial strength and sheet migration

Jeanne M. Quinn[1]*, Yuou Wang[1]*, Megan Wood[1]*, Annette S. Flozak[1], Phuong M. Le[1], Alex Yemelyanov[1], Patrick W. Oakes[3] and Cara J. Gottardi[1,2]**

[1]Department of Pulmonary Medicine, [2]Cell & Developmental Biology,

Northwestern University

Feinberg School of Medicine, Chicago, IL 60611

[3]Department of Cell & Molecular Physiology,

Loyola University Chicago Stritch School of Medicine,

Maywood, IL 60153

*Co-first authorship

**Corresponding Author: Cara J. Gottardi
Northwestern University Feinberg School of Medicine
303 Superior St., Simpson-Querrey Institute, 5-525
Chicago, IL 60611
Office Phone: (312) 503-4123

Jeanne M. Quinn ORCID: 0000-0002-7830-4659

Yuou Wang ORCID: 0000-0001-8675-8055

Patrick W Oakes ORCID: 0000-0001-9951-1318

Cara J. Gottardi ORCID: 0000-0003-0912-7617

Email: c-gottardi@northwestern.edu

Condensed title: α-cat catch-bond in wound repair

Character/Word count: 36,942 (Excluding References/Fig. Legends)

ABSTRACT (214 Words)

α-catenin (α-cat) displays force-dependent unfolding and binding to actin filaments through direct and indirect means, but features of adherens junction structure and function most vulnerable to loss of these allosteric mechanisms have not been directly compared. By reconstituting an α-cat F-actin-binding domain unfolding mutant known to exhibit enhanced binding to actin (α-cat-H0-FABD$^+$) into α-cat knock-out Madin Darby Canine Kidney (MDCK) cells, we show that partial loss of the α-cat catch bond mechanism (via an altered H0 α-helix) leads to stronger epithelial sheet integrity with greater co-localization between the α-cat-H0-FABD$^+$ mutant and actin. α-cat-H0-FABD$^+$ -expressing cells are less efficient at closing scratch-wounds, suggesting reduced capacity for more dynamic cell-cell coordination. Evidence that α-cat-H0-FABD$^+$ is equally accessible to the conformationally sensitive α18 antibody epitope as WT α-cat and shows similar vinculin recruitment suggests this mutant engages lower tension cortical actin networks, as its M-domain is not persistently open. Conversely, α-cat-M-domain salt-bridge mutants with persistent recruitment of vinculin and phosphorylated myosin light chain show only intermediate monolayer adhesive strengths, but display less directionally coordinated and thereby slower migration speeds during wound-repair. These data show α-cat M- and FABD-unfolding mutants differentially impact cell-cell cohesion and migration properties, and suggest signals favoring α-cat-cortical actin interaction without persistent M-domain opening may improve epithelial monolayer strength through enhanced coupling to lower tension actin networks.

INTRODUCTION

α-catenin (α-cat) is a central mechanosensitive scaffold molecule that links the cadherin-catenin complex to the cortical actin cytoskeleton at adherens junctions (AJs), where the latter form structural units essential for tissue morphogenesis and homeostasis (Green et al., 2010; Harris and Tepass, 2010). α-cat mechanosensitivity depends on the conformations and binding activity of its three bundled alpha helical domains (Ishiyama et al., 2013; Rangarajan and Izard, 2012). The N-terminal domain comprises two 4-helical bundles, where the former binds β-catenin (Pokutta and Weis, 2000). The C-terminal domain engages actin through a 5-helical bundle, where force-dependent alteration of the first helix favors high affinity F-actin binding and catch-bond behavior (Buckley et al., 2014; Ishiyama et al., 2018; Wang et al., 2022; Xu et al., 2020). The middle (M)-region of α-cat comprises three 4-helical bundles (M1-3), which undergo sequential unfurling events, M1 at ~5pN forces followed by M2-M3 at ~12pN forces, to recruit α-cat M-domain binding partners in a force-dependent manner (Barrick et al., 2018; Kim et al., 2015; Li et al., 2015; Maki et al., 2018; Pang et al., 2019; Seddiki et al., 2018; Terekhova et al., 2019; Thomas et al., 2013; Yao et al., 2014; Yonemura et al., 2010). As such, α-cat is now understood to be a mechanosensitive protein that links acto-myosin force thresholds to distinct α-cat conformational states and partner recruitment. However, the particular adhesive processes and coordinated behaviors that critically depend on α-cat mechanosensitivity are only just emerging (Cho et al., 2022; Donker et al., 2022; Matsuzawa et al., 2018; Monster et al., 2021; Nishimura et al., 2022; Noordstra et al., 2023; Sarpal et al., 2019; Sheppard et al., 2023; Twiss et al., 2012; van den Goor and Miller, 2022).

Our team previously sought to understand the α-cat catch-bond mechanism through a structure-rationalized mutation approach (Ishiyama et al., 2018). By altering 4 amino acids (RAIM to GSGS, a.a. 666-669) in a kinked portion of the first alpha-helix of the α-cat actin-binding domain, Ishiyama et al generated an α-cat with ~3-fold enhanced F-actin binding *in vitro,* suggesting a model for how acto-myosin forces could alter this region and promote strong actin-binding in cells (Ishiyama et al., 2018). Two recent studies extend and refine this model, implicating the entire first α-helix as a force-gate for F-actin binding, where full loss of this domain (a.a. 666-698) leads to substantially higher actin-binding in vitro (18-fold) (Xu et al., 2020), converting a two-state catch bond into a one-state slip bond (Wang et al., 2022). To accommodate these new findings, we now refer to the Ishiyama et al RAIM → GSGS unfolding

mutant as α-cat-H0-FABD$^+$, where H0 refers to a short α-helix preceding the first long helix of the α-cat actin-binding domain. This revised nomenclature allows the field to avoid confusion with the α-cat-ΔH1 mutant of Wang et al (2022), which removes both H0 and H1. Since the α-cat-H0-FABD$^+$ mutant fails to rescue embryonic lethality of zygotic *αCat* null mutant flies, we know this partial catch-bond mechanism is critical for tissue morphogenesis (Ishiyama et al., 2018). But the specific features of AJ structure and epithelial properties most sensitive to partial loss of α-cat-ABD F-actin catch-bond behavior are less clear, but important in understanding benefits of such regulation for tissue homeostasis. While our previous work showed that expression of α-cat-H0-FABD$^+$ in α-cat-negative R2/7-variant DLD1 human colon carcinoma cells leads to epithelial monolayers more resistant to shear-forces, but less efficient at wound repair (Ishiyama et al., 2018), the generality and robustness of these findings remain untested.

In the current study, we generalize these findings to another epithelial cell line, Madin Darby Canine Kidney (MDCK). We demonstrate that partial loss of the α-cat catch bond mechanism (via an H0 α-helix unfolding mutant, RAIM → GSGS) leads to stronger epithelial sheet integrity with greater co-localization between α-cat-H0-FABD$^+$ and F-actin, consistent with this mutant's enhanced association with F-actin under solution-binding centrifugation conditions. However, α-cat-H0-FABD$^+$ -expressing cells are less efficient at closing scratch-wounds or uniformly packing, suggesting reduced capacity for more dynamic cell-cell coordination. These results imply that cell signals (heretofore unknown) that serve to increase the α-cat/cortical actin interaction might increase epithelial cohesion, but with the cost of limiting cell-cell coordination required for epithelial barrier repair. In addition, while the α-cat/F-actin catch-bond mechanism is thought to be required for M-domain unfolding and partner recruitment, we show that the α-cat-H0-FABD$^+$ unfolding mutant is not functionally equivalent to α-cat-M-domain salt-bridge mutants. Indeed, while the latter shows weaker cohesive strength than the former using a standard monolayer fragmentation assay, α-cat-M-domain salt-bridge mutants more strongly perturb the dynamic process of epithelial sheet migration. These data may shed light on how α-cat M-domain missense mutations contribute to epithelial defects that lead to disease (Saksens et al., 2016; Tanner et al., 2021).

127 **RESULTS**

128

129 **An α-cat CRISPR knock-out MDCK cell system to interrogate a α-cat mutant function**

130 To more broadly understand how α-cat force-dependent actin binding contributes to epithelial
131 junction organization and function, we sought to generalize previous efforts with a "force-
132 desensitized" α-cat actin-binding mutant (Ishiyama et al., 2018) to the non-cancerous kidney
133 epithelial cell line, MDCK (Madin Darby Canine Kidney), a widely used cell line in the cell-cell
134 adhesion field. We established α-cat knock-out (KO) MDCK cells using the CRISPR-Cas9
135 system for reconstitution with wild-type or mutant forms of α-cat. We generated RNA guides to
136 α-cat sequences in exons 2 and 4 (Fig. 1A). After transfection and drug selection, single
137 colonies were expanded and screened for lack of α-cat expression. No full length α-cat was
138 detected in knock-out clones by immunoblot analysis (Fig. 1B). Since an immuno-reactive lower
139 molecular weight species was more prominent in clones generated by the most N-terminal
140 guide (gRNA.5), we stably expressed WT α-cat or α-cat-H0-FABD^{+} in the α-cat KO2.2 clone,
141 which expressed this form least. We now know this lower molecular weight species corresponds
142 to a form of α-cat lacking its N-terminal region, likely consequent to our CRISPR-insertion-
143 deletion (INDEL) strategy, which commonly leads to internal ribosome entry and alternative
144 protein products (Tuladhar et al., 2019). As this α-cat isoform lacks the β-cat binding domain
145 and fails to associate with the cadherin-catenin complex, we moved forward with this cell
146 system nonetheless, reasoning this α-cat form cannot directly participate in the cadherin-catenin
147 catch-bond mechanism. Other possible functions of this α-cat isoform expressed at levels seen
148 for guide RNA.5 and generation of complete α-cat null MDCK clones will be described
149 elsewhere (Flozak et al., in preparation). Regardless, the low levels of α-cat variant seen with
150 guide RNA.2 does not obviously localize to cell-cell contacts (Fig. S1A), and restoration of α-cat
151 KO clone 2.2 with α-cat-GFP largely rescues the MDCK parental phenotype and monolayer
152 adhesive strength (Fig. S1B, gray bars).

153

154 **An α-cat actin-binding domain unfolding mutant with enhanced actin binding increases**
155 **epithelial sheet integrity**

156 Flow sorting the brightest third of α-cat-RFP or -GFP expressing cells (not shown), we
157 generated pooled "polyclonal" cell lines to avoid sub-clone variation. Both RFP and GFP-tagged
158 α-cat proteins were expressed similar to normal α-cat levels seen in parental MDCK cells (Fig.
159 1C-D). Modestly lower expression of RFP-tagged α-cat proteins may be due to expression from
160 different plasmid promoters (Methods). Consistent with evidence that this α-cat-H0-FABD$^+$
161 (RAIM→GSGS) unfolding mutant favors F-actin binding *in vitro* (Ishiyama et al., 2018), we
162 found that MDCK α-cat-KO2.2 cell monolayers reconstituted with α-cat-H0-FABD$^+$-GFP
163 remained intact upon mechanical disruption, whereas WT αCat-GFP restored monolayers
164 dispersed into numerous fragments (Fig. 1E-F). These data are consistent with previous work
165 showing that α-cat-H0-FABD$^+$ enhances monolayer resistance to mechanical disruption in a
166 human colon cancer cell line (Ishiyama et al., 2018), and generalize the rule that increased α-
167 cat cortical actin interactions can improve the strength of epithelial sheets across tissue types.

168

169 **α-cat-H0-FABD$^+$ shows enhanced colocalization with F-actin**

170 Restoration of α-cat-KO MDCK cells with a "force-insensitive" mutant that interrupts α-cat
171 Middle-domain salt-bridge interactions (M319G/R326E) led to enhanced recruitment of F-actin
172 and myosin to cell-cell junctions, presumably via α-cat M-domain binding partners that reinforce
173 and amplify acto-myosin contractility (Matsuzawa et al., 2018). Whether a force-desensitized α-
174 cat-H0-FABD$^+$ with enhanced actin-binding drives similar actin enrichment at junctions is not
175 known. To address this, α-cat KO2.2 cells restored with WT α-cat-RFP or α-cat-H0-FABD$^+$-RFP
176 were grown on porous filters for 10 days before fixing and staining with phalloidin. Curiously,
177 these high-density cultures revealed non-overlapping patches of WT α-cat and F-actin signal,
178 whereas the α-cat-H0-FABD$^+$ mutant showed smoother alignment (Fig. 2A). Line-scan analysis
179 of representative bicellular junctions (yellow lines) revealed clear spatial segregation of WTα-cat
180 from F-actin, whereas the α-cat-H0-FABD$^+$ mutant distributed more uniformly along F-actin (Fig.
181 2B). Analysis of full z-stacks confirms greater colocalization of α-cat-H0-FABD$^+$ mutant and F-
182 actin compared with WTα-cat (Fig. 2C). Despite the improved colocalization between α-cat-H0-
183 FABD$^+$ and F-actin, total actin levels appeared unaltered in WTα-cat-RFP/α-cat-H0-FABD$^+$ -
184 GFP co-cultures (Fig. 2D, x-z views, phalloidin in grayscale). Orthogonal views also showed that
185 while WTα-cat-RFP could apically enrich at the zonula adherens junction (Fig. 2D, x-z views,
186 magenta arrows), α-cat-H0-FABD$^+$ -GFP was distributed more evenly along the lateral

membrane, coinciding with F-actin localizations (Fig. 2D, x-z views, green arrows). Together, these data suggest that the α-cat-H0-FABD$^+$ mutant likely enhances monolayer cohesion by better engaging actin filaments that run along the entire length of the cell-cell contact. Conversely, the WT α-cat may be tuned to ignore this pool of actin, engaging only with filaments under higher tension thresholds (e.g., at zonula adherens).

α-cat M1 and M2-domains are not persistently accessible in α-cat-H0-FABD$^+$

Single molecule stretch measurements along with steered molecular dynamic simulations reveal how the α-cat M-domain may sequentially unfurl under distinct force thresholds (Leckband and de Rooij, 2014; Li et al., 2015; Yao et al., 2014). In cells, this M-domain unfurled state has been conveniently detected by the monoclonal antibody, α18, which recognizes an M2-helix (a.a. 420-430) preferentially accessible at tension-bearing versus more relaxed cell-cell adhesions (Nagafuchi et al., 1994; Yonemura et al., 2010). Indeed, a previous study revealed the M-domain "activated" salt-bridge mutant (M319G/R326E) was substantially more accessible to α18 than WTα-cat (Matsuzawa et al., 2018). To address the extent to which α-cat-H0-FABD$^+$ favors greater accessibility to α18, we co-cultured α-cat-H0-FABD$^+$-GFP with WT α-cat-RFP and stained for α18. We find that while α18 can recognize α-cat-H0-FABD$^+$ better than WT α-cat in some regions of the monolayer (Fig. 3A), other regions showed preferential recognition of WT α-cat by α18 (Fig. 3B), suggesting α18 accessibility differences between α-cat-H0-FABD+ and WT α-cat are more likely driven by the complex and variable tension forces experienced by the monolayer. We also fail to see constitutive recruitment of vinculin to apical junctions of α-cat-H0-FABD+-expressing cells, where vinculin is known to display tension-dependent recruitment to an α-cat helical region of the M1-domain (Fig. 3C-D) (Hirano et al., 2018; Yao et al., 2014). Collectively, these data reveal that the α-cat M1 and M2-domains are not constitutively accessible in α-cat-H0-FABD$^+$, despite its better colocalization with actin and improved monolayer integrity (Figs. 2A and 1E). These data raise the possibility that the α-cat-H0-FABD$^+$ mutant engages lower-tension cortical actin networks in dense MDCK monolayers, where these actin networks may be typically ignored by WT α-cat.

α-cat-H0-FABD$^+$ interferes with normal cell-cell packing

217 MDCK cells are often used in epithelial biology for their consistent high-density packing on
218 filters, as evidenced by the normal distribution of apical membrane sizes (Fig. 4A, left).
219 Curiously, MDCK reconstituted with α-cat-H0-FABD$^+$ manifest greater heterogeneity in apical
220 membrane size, with small and large sizes often sharing cell-cell contact (Fig.4A, right).
221 Histogram and Kolmogrov-Smirnov analysis reveal α-cat-H0-FABD$^+$ alters the distribution of
222 apical areas (Fig. 4B & 4C), despite no significant mean apical areas difference between WT α-
223 and α-cat-H0-FABD$^+$ (Fig. 4C). Since this phenomenon can occur in the context of actomyosin
224 contractility differences between adjacent cells (Armon et al., 2018; Matsuzawa et al., 2018),
225 these data suggest an α-cat that is able to engage both lower- and higher-tension actin
226 filaments may be sufficient to propagate signaling relationships that support this irregular cell-
227 packing state.

228 **α-cat-H0-FABD$^+$ limits epithelial sheet wound closure**

229 We previously reported that the α-cat-H0-FABD$^+$ mutant interferes with wound-front migration
230 using the R2/7 DLD1 cell system (Ishiyama et al., 2018), but whether this also holds for MDCK
231 cells, reflecting a generalized phenomenon is unknown. Live imaging of scratch-wound reveals
232 that α-cat-H0-FABD$^+$ mutant cells display unproductive cell-cell tugging orthogonal to the
233 direction of migration (Fig. 5A), leading to reduced wound area closure than WT α-cat (Fig. 5B-
234 C, Movie 1). Finger-like tubular membrane structures, which form via invagination at the
235 interface of leader and follower cells to coordinate directional migration (Hayer et al., 2016),
236 were prominently detected in both WT α-cat and α-cat-H0-FABD$^+$ monolayers (Fig. 5A). While
237 some α-cat-H0-FABD$^+$ tubular structures appeared less dynamic and more persistent than WT
238 α-cat (Fig. S2A), there was no significant difference in their number or length (Fig. S2B-C, n =
239 ~50 structures). Interestingly, a greater number of tubular invaginations in α-cat-H0-FABD$^+$
240 wound fronts were angled perpendicularly to the direction migration, consistent with the more
241 uncoordinated (side-to-side) movements of α-cat-H0-FABD$^+$ cells relative to WT α-cat (Fig. 5D;
242 S2D-E). These data demonstrate that normal α-cat catch-bond behavior is required for efficient
243 epithelial sheet migration, through favoring a more directional (front-to-back) migration.

244 **α-cat-Middle and F-actin-binding domain unfolding mutants are not equivalent in**
245 **epithelial monolayer disruption and sheet migration assays**

246 α-cat M-domain "activated" salt-bridge mutants show enhanced recruitment of a number of
247 actin-binding proteins, such as vinculin, afadin and likely others (Matsuzawa et al., 2018;

248 Sakakibara et al., 2020). While destabilization of α-cat M-domain salt-bridges can disrupt
249 epithelial sheet migration (Matsuzawa et al., 2018 ; Seddiki et al., 2018), the degree to which α-
250 cat M-domain and actin-binding "catch-bond" unfolding mutants are functionally redundant or
251 distinct is not known. To address this question, we compared α-cat M-domain salt-bridge and
252 H0-mutant α-catenins head-to-head using intercellular adhesion and barrier-release assays.
253 Although α-cat constructs with fluorescent-tags placed at the carboxyl-terminus can rescue full
254 development of αCat-null flies (Sarpal et al., 2012), evidence that the unstructured C-terminal
255 extension also contributes to force-activated actin binding (Mei et al., 2020), along with
256 knowledge the extreme C-terminus of α-cat contains a PDZ-interaction motif that might interfere
257 with adherens junction functions, obliged us to generate α-cat mutants tagged with monomeric
258 GFP at the N-terminus. We first affirmed that the N-terminal GFP-tagged α-cat-H0-FABD^{+}
259 migrates more slowly than GFP-α-cat WT cells, similar to α-catenins tagged at the C-terminus
260 (Fig. 6A). While these barrier-release migration differences did not reach statistical significance
261 (p = 0.0664 and 0.0565), they supported scratch-wound data showing an inhibitory role (Fig. 5).
262 The generally faster migration of C-terminally tagged α-catenins may be due to their 2-3 fold
263 higher expression than N-terminally tagged α-catenins (Fig. S3A). Interestingly, our N-terminally
264 tagged unfolding mutants are functionally distinct despite their similar expression by
265 immunoblotting (Fig. S3): While the α-cat H0-mutant shows stronger cohesion than α-cat M-
266 domain salt-bridge mutants (particularly the aspartate to alanine DDD>AAA mutant), the latter is
267 the most potent inhibitor of epithelial sheet migration (Fig 6B). Analysis by particle image
268 velocimetry (PIV) reveals that this due to reduced migratory capacity is associated with less
269 directed and coordinated movements (Fig. 7; Figs S4). Generally, differences in vector speed
270 and direction (Cos theta) were not distinguishable with the first 4-hours of migration, but
271 developed over time with all α-cat mutants significantly differing from WT-α-cat (Fig. 7B-E).
272 Interestingly, α-cat-H0-FABD^{+} monolayers, despite being the most cohesive (Fig. 6C), migrated
273 significantly faster than both α-cat M-domain salt-bridge mutants (KRR and DDD) at later time
274 points (Fig. 7C-D). While α-cat-H0 monolayers showed reduced final speed and correlation
275 across the monolayers compared to WT (Fig. 7E, p = **** by multiple comparisons), H0
276 monolayers initially demonstrated the largest range of correlated movement compared to WT
277 and M-domain mutants (Fig. 7F, p = **** by multiple comparisons). Spatial correlation
278 increased most in WT monolayers (Fig. 7E-F), coinciding with general velocity and angle trends,
279 suggesting the FABD+ and M-domain mutants do not cohesively 'respond' over time like WT

280 monolayers. We noticed that one of our α-cat M-domain salt-bridge mutants (DDD) was
281 particularly potent at inhibiting cell migration (Fig. 7B-E), despite targeting amino acids
282 comprising the KRR salt-bridge pair. While both α-cat M-domain salt-bridge mutants show
283 enhanced recruitment of vinculin, confirming their persistently unfolded state, the DDD mutant
284 showed greater recruitment of vinculin than the KRR mutant (Fig. 8; Fig. S5), offering a possible
285 explanation for different migration characteristics. α-cat M-domain salt-bridge mutants also
286 show increased junctional enrichment in phosphorylated myosin light chain, particularly at
287 tricellular junctions (Fig. 9; Fig. S6, MyoIIA was unchanged, not shown), which may further
288 contribute to less coordinated cellular flows. Together, these data suggest α-cat mutants that
289 favor M-domain unfolding or enhanced actin binding are not equivalent, where M-domain
290 unfolding appears most perturbing to cohesive migration.

291

Discussion

A number of single molecule studies have shown that α-cat binding to F-actin is force-dependent (Arbore et al., 2022; Buckley et al., 2014; Mei et al., 2020), where the first extended α-helix (H0-H1) of α-cat's 5-helical bundle actin-binding domain negatively regulates (i.e., force-gates) actin-binding (Ishiyama et al., 2018; Wang et al., 2022; Xu et al., 2020). However, the features of epithelial junction organization and dynamic cell behaviors that critically depend on α-cat/FABD$^+$ catch-bond activity remain unclear. Also unclear is the degree to which M- and FABD unfolding mutants manifest distinct consequences for static versus dynamic epithelial adhesive processes. While our previous work showed that restoring α-cat-H0-FABD$^+$ in an α-cat-negative colon carcinoma cell line led to epithelial monolayers more resistant to shear-forces, but less efficient at wound repair (Ishiyama et al., 2018), the generality and robustness of these phenotypes remained untested. Here, we extend these findings to the MDCK epithelial cell line. We show that partial loss of the α-cat catch bond property (via an altered H0 α-helix) leads to stronger epithelial sheet integrity with greater co-localization between α-cat-H0-FABD$^+$ and F-actin, presumably due to the latter's persistent association with lower tension cortical actin networks. Since α-cat-H0-FABD$^+$ -expressing cells are less efficient at closing scratch-wounds or uniformly packing at high density, this mutant displays reduced capacity for dynamic cell-cell coordination. These results reinforce the idea that the α-cat catch bond mechanism is most critical for dynamic rather than static cell-cell adhesions. These results further imply an interesting trade-off; cell signals (heretofore unknown) that serve to reduce the force-sensitivity of the α-cat/cortical actin interaction might improve epithelial monolayer strength through enhanced binding to lower tension cortical actin networks. Indeed ,these lower tension actin networks may comprise the bulk of cortical actin in mature epithelial monolayers. But such signals would render α-cat less selective of acto-myosin filaments under higher force, extracting a cost for more dynamic cell migrations, which depend on α-cat ignoring the lower tension actin networks.

A limitation of relying on the α-cat-H0-FABD$^+$ mutant to infer α-cat catch-bond activity in cells is the current lack of information on its force-dependent activity using optical trap single molecule analyses (Fig. S7). WT α-cat manifests two-state binding to actin: low or no binding under low forces, binding under mid-forces and slippage under high forces (Arbore et al., 2022; Buckley et al., 2014). Recent studies suggest this two-state model property implicates both H0 and H1, but

largely centers on the longer H1 helix (Mei et al., 2020; Wang et al., 2022; Xu et al., 2020). Deletion of both helices (ΔH0-H1 ABD) leads to greatly enhanced actin binding in solution (18-fold; (Xu et al., 2020) and longer binding lifetimes under low forces, but "slippage" at mid-range forces (Wang et al., 2022). As the α-cat-H0-FABD$^+$ mutant shows more modest 3-4-fold increase in F-actin binding affinity *in vitro* (Ishiyama et al., 2018) versus 18-fold (Xu et al., 2020), it is likely this mutant still manifests two-state catch bond activity, as the vinculin ABD also lacks H0 yet nonetheless forms catch-bonds with actin (Bakolitsa et al., 2004; Bakolitsa et al., 1999; Borgon et al., 2004; Huang et al., 2017). We reason, therefore, that the α-cat-H0-FABD$^+$ mutant has an increased bond lifetime with actin under lower force thresholds in cells. This model is supported by the enhanced colocalization of α-cat-H0-FABD$^+$ with lateral membrane F-actin compared with WT α-cat, where the latter accumulates along basolateral membrane patches that exclude actin (Fig. 2). Moreover, evidence M1 and M2-domains are not constitutively accessible to vinculin or the α18 epitope in α-cat-H0-FABD$^+$ compared with WT α-cat, further supports the idea that α-cat-H0-FABD$^+$ largely engages lower tension cortical actin networks (Fig. 10A, Schematic). Thus, we speculate the α-cat-H0-FABD+ mutant behaves as a "force-desensitized" form of α-cat in epithelial cells, but the particular force-sensitive profile of this mutant and whether it affects the magnitude of the catch-bond behavior will require future testing.

We were intrigued that cells expressing the α-cat-H0-FABD$^+$ mutant led to non-normal packing distribution of MDCK cells grown to high density on filters, where cells with small apically constricted junctions were directly connected to seemingly larger flatter cells (Fig. 4A). While this phenotype may also be related to α-cat expression levels and GFP-tag placement, it is worth noting that tissues can adopt this packing state under different conditions (Armon et al., 2018) and via altered expression of junction proteins and signaling relationships that impact apical contractility (Hildebrand, 2005; Matsuzawa et al., 2018; Sakakibara et al., 2020). Evidence here suggests the possibility that an α-cat with enhanced binding to lower tension actin networks with possible slippage under higher forces may be sufficient to propagate similar cell-cell relationships.

354 A recent study found MCF7 α-cat KO cells reconstituted with α-cat H0-FABD$^+$ showed
355 enhanced adherens junction assembly during the last step of epithelial wound-front closure,
356 where “head-on” junction establishment was associated with reduced lamellipodial activity and
357 cortical actin flow (Noordstra et al., 2023). Interestingly, unliganded surface E-cadherin moved
358 faster in MCF7 cells reconstituted with α-cat H0-FABD$^+$, with no change in the overall speed of
359 cortical actin flow. We speculate this enhancement in α-cat H0-FABD$^+$ cortical flow may be due
360 to increased binding to lower tension actin networks, which at nascent cell-cell contacts allows
361 for a greater number of actin-engaged cadherin-catenin complexes to drive adherens junction
362 formation.

363 Lastly, α-cat is long known to bind F-actin directly or indirectly through force-dependent
364 recruitment of other actin-binding proteins, such as vinculin, but the degree to which these
365 modes of actin-binding are redundant or distinct has not been directly tested. By comparing α-
366 cat H0-FABD$^+$ and α-cat M-domain salt-bridge mutants head-to-head in epithelial sheet
367 disruption and barrier-release migration assays, we show that M-domain unfurling is more
368 disruptive to adhesion and migration than enhancement of F-actin binding. This finding is
369 notable and may be related to evidence that familial missense mutations that cause Macular
370 Pattern Eye Dystrophy exclusively localize to the M-domain (Saksens et al., 2016; Tanner et al.,
371 2021), underscoring the importance of this domain to normal α-cat function. Future work will be
372 required to understand the force-sensitive targets of α-cat M-domain unfolding or dysfunction
373 that negatively impact coordinated epithelial cell behaviors (Fig. 10B, Schematic).

ACKNOWLEDGEMENTS

This work relied on the following Northwestern University services and core facilities: Flow Cytometry (NCI CA060553); Center for Advanced Microscopy (NCI CCSG P30 CA060553) and Skin Biology and Diseases Resource-based Center (P30AR075049) from the NIAMS. We thank Pankaj Bhalla for gene editing advice with help from the SBDRC GET iN Core.

FUNDING

JMQ was supported by T32 HL076139; PWO is supported by NIH GM148644. CJG is supported by NIH GM129312 and HL163611. All authors declare no competing financial interests.

Author contributions: JMQ, MNW, ASF , PML and AY conducted experiments and analyzed results; PWO advised and wrote code for the PIV analysis; CJG designed and supervised the study. JMQ, YW, PWO and CJG wrote the manuscript. PWO and CJG provided funding for project.

389 **METHODS**

390 *Plasmid generation and constructs*

391 The αE-catenin cDNA was amplified by PCR and subcloned into either a modified pcDNA3.1
392 vector (Ishiyama et al., 2010) to express αE-catenin-mRFP or a modified pCAN vector (Ichii
393 and Takeichi, 2007) to express αE-catenin-mEGFP (EGFP with the dimerization-disrupting
394 A206K mutation (Zacharias, 2002). N-terminally tagged αE-catenins were synthesized by
395 VectorBuilder using a dimerization-disrupted mEGFP (A206K) in third-generation lentiviral
396 vectors with components pLV[Exp]-CMV>mEGFP-αE-catenin EF1A(core)>Puro. Lentivirus
397 packaging (psPAX2, #12260) and envelope (pMD2.G, #12259) plasmids were purchased from
398 Addgene.

399

400 *Cell culture and stable cell line selection*

401 MDCK II cells were maintained in Dulbecco's Modified Eagle's Medium (DMEM, Corning),
402 containing 10% fetal bovine serum (FBS, Atlanta Biologicals or JRS Scientific), 100 U/ml
403 penicillin and 100 μg/ml streptomycin (Corning). α-cat/*Ctnna1* knockout MDCK cells were
404 generated using CRISPR-Cas9 system, RNA guides were designed targeting α-cat sequences
405 in exons 2 and 4. Guide RNA (gRNA) targeting different canine *CTNNA1* exons were designed
406 with CHOPCHOP online tools (Labun et al., 2019). Sequences of oligonucleotides were as
407 follows: 5'-GAAAATGACTTCTGTCCACACAGG -3' (exon 2, covering the MTSVHTG protein
408 sequence) and 5'-AGTCTAGAGATCCGAACTCTGG -3' (exon 2, covering the SLEIRTLA
409 sequence). Single guide RNA (sgRNA), Cas9 nuclease (HiFi) and duplex buffer were purchased
410 from Integrated DNA Technologies. RNAs were reconstituted and diluted to 5 μM with duplex
411 buffer; Cas9 protein to 10 μM with PBS. MDCK cells were plated in 12-well plates at a seeding
412 density of 1.0 x 10^5 cells in 1 mL DMEM-complete a day before. For one reaction, sgRNA (20
413 μL), Cas9 (15 μL), DMEM (30 μL, no serum and antibiotics) and Lipofectamine RNAiMax (4 μL,
414 Invitrogen) were mixed and incubated at room temperature for 20 min. The complex was treated
415 to the cells in complete medium and incubated overnight at 37 ^{o}C and 5% CO_2. The medium
416 was changed and the cells were allowed to recover for one day. Cells were split to maintain 30-
417 50% confluency. The sgRNA-Cas9 treatment was repeated 3 times. Cells were expanded and
418 sorted with a flow cytometer (FACSMelody, BD) to 96-well plates to grow single cell colonies.
419 The colonies were screened for low (< 5 ng/well at confluent) α-cat expression using a α-cat C-

420 terminal antibodies. The selected colonies were verified with western blot. Knockout cell line
421 (2.2 clone) was chosen based on lowest level of α-cat isoform lacking N-terminal sequences.

422

423 After transfection and drug selection, colonies were expanded and screened for lack of α-cat
424 expression. Cells were transfected with expression vectors by using Lipofectamine 3000
425 (ThermoFisher Scientific), and cells with stable protein expression was selected based on
426 antibiotic resistance (100 µg/mL Zeocin for pcDNA3.1 and 300 µg/mL hygromycin for pCAH
427 vectors) and subsequently isolated by flow cytometry. For lentivirus production, 293T cells
428 (GeneHunter) were transfected with 8ug expression vector (Vector Builder), 6μg psPAX2, and
429 2μg pMD2.G using TransIT (Mirus). Viral supernatant was collected 48 and 72h after
430 transfection, passed through a 0.45μm filter, and supplemented with 1μL/mL polybrene (Sigma).
431 To generate stable GFP-α-cat lines, MDCK α-cat KO cells were transduced for 6hr at 37°C on
432 10cm plates with 2mL prepared viral supernatant. Cells were selected in culture media
433 containing 5μg/mL puromycin, then sort-matched for GFP using a FACSMelody 3-laser sorter
434 (BD).

435 *Antibodies*

436 The following primary antibodies were used: polyclonal rabbit anti-α-cat (C3236, Cell Signaling),
437 hybridoma mouse anti-α-catenin (5B11, (Daugherty et al., 2014)), Rat anti-α-catenin mAb (α18)
438 was a kind gift of Dr. A. Nagafuchi (Nara Medical University, Nara, Japan), rabbit anti-GAPDH
439 (Cat# sc-25778, Santa Cruz, now discontinued), polyclonal rabbit anti-GFP (A11122, Invitrogen)
440 and Phalloidin-488 or -568 (A12379, Invitrogen). Secondary antibodies for Western blotting
441 included HRP-conjugated goat anti-mouse and -rabbit antibodies (Bio-Rad), or fluorescently
442 labeled donkey anti-mouse and -rabbit antibodies (680RD or 800RD, LiCor Biosciences).
443 Secondary antibodies for immunofluorescence included IgG Alexa Fluor 488 or 568-conjugated
444 goat anti-mouse or -rabbit antibodies (Invitrogen).

445

446 *Immunofluorescence and Imaging*

447 Cells were grown on cell culture inserts (Falcon), fixed in 4% paraformaldehyde (Electron
448 Microscopy Services, Hatfield, PA) for 15', quenched with glycine, permeabilized with 0.3%
449 Triton X-100 (Sigma), and blocked with normal goat serum (Sigma). Primary and secondary

450 antibody incubations were performed at RT for 1h, interspaced by multiple washes in PBS, and
451 followed by mounting coverslips in ProLong Gold fixative (Life Technologies). Images of α-cat,
452 F-actin, and vinculin localizations were captured with Nikon A1R Confocal Laser Point Scanning
453 microscope using NIS Elements software (Nikon) with GaAsP detectors and equipped with 95B
454 prime Photometrics camera, Plan-Apochromat 60x/1.4 objective. Confocal Z-stacks were taken
455 at step size of 0.3μm.

456

457 *Image Analysis and Fluorescence Quantification*

458 To examine the localization of vinculin and α-cat, junctional enrichment was quantified on single
459 apical slices in FIJI and normalized. Briefly, the integrated signal intensity from 1μm circular
460 ROIs were measured from bicellular junctions (BCJ) and the adjacent cytoplasm (Cyto). Cyto
461 signal was subtracted from BCJ signal, and the enrichment was normalized to 1 within each
462 experimental group. Junctional phospho-myosin was similarly quantified, but enrichment was
463 taken over FOV signal to minimize the contribution of background cytosolic antibody signal. To
464 compare the distribution of F-actin and α-cat along junctions, 0.1μm circular ROIs were placed
465 along BCJs and the integrated signal intensity was measured from both channels. The
466 junctional signal was standardized to the FOV signal and normalized to 1. Normalized F-actin
467 vs. α-cat signal for each ROI was plotted, and correlation was measured with Pearson's "R"
468 value and by linear fit. F-actin vs α-cat signal is further reported with a typical line-scan analysis
469 taken along a BCJ indicated in the figure panel.

470

471 *Scratch Wound Assay*

472 MDCK cells (250,000) were plated for 24hr on LabTek #1 4-well chamber slide (43300-776,
473 Thermo Scientific), wounded with a P200 micropipette tip and allowed to recover for 2hr. Prior to
474 imaging, DMEM media was replaced with FluoroBright DMEM (Life Technologies) and 10
475 μg/mL Mitomycin C (Sigma) to limit cell proliferation. Cells in Figure 5 were imaged with the 20x
476 objective every 10 min (both phase contrast and fluorescent channels) on the Nikon Biostation
477 IM-Q with the slide holder module (located in Nikon Imaging Facility) at 37°C, 5% CO_2, for 15 hr.
478 6 fields of view (FOV) were captured along the wound edge. To quantify change in wound area,
479 the resulting .ids file was imported to ImageJ, and the wound edge of the phase-contrast image
480 was traced with the polygon tool at time = 0 and time = 15hr. The area of the resulting polygon

481 was measured in pixels² and the resulting data were compared by performing One-way ANOVA
482 statistical analysis followed by Tukey's multiple comparison test using GraphPad. Images
483 presented in the paper were adjusted for brightness/contrast but were otherwise unprocessed.
484 Individual cell tracks were visualized using the MTrackJ plug-in (FIJI) (Fig. S2E). Cadherin
485 fingers were counted manually and within 150-minutes after wounding. Length, intensity &
486 angles were measured using FIJI by using the line tool (line width of 3 pixels) along the cadherin
487 fingers at 200% zoom.

488

489 *Epithelial barrier-release assay*

490 Cells (30,000 and 60,000) were plated to 35mm 4-well Ibidi plates (#80466) at for 48h. Two
491 hours before imaging, the barrier was pulled, and media was changed to DMEM-10%FBS with
492 10μg/ml mitomycin C for 2 hours incubation. Media was changed to Fluorobrite media with 10%
493 FBS. Positions were selected along the wound edge and brightfield images were acquired at
494 10-minute intervals over 16h hours on a Nikon Ti2 microscope using a 20x air objective. The
495 monolayers' coordinated movement was further analyzed by Particle Image Velocimetry (PIV)
496 on background-masked timelapses.

497

498 *Particle Image Velocimetry (PIV) and Flow Analysis*

499 To analyze the collective motion of migrating cells during barrier release assays, we performed
500 particle image velocimetry (PIV) measurements using code from openpiv (Liberzon et al., 2021).
501 Briefly, the original image was broken down into a series of small windows that covered the
502 entire image. The displacement of each window between successive frames was determined by
503 performing a cross-correlation. This resulted in a vector field encoding the local movement of
504 objects in the image. For this analysis we used a window size of 90x90 pixels (33x33 μm) and a
505 slightly larger search window size of 93 pixels. Each window overlapped by 65 pixels (~24 μm),
506 resulting in a grid that produced a displacement vector every 28 pixels (~10 μm– approximately
507 the size of a single cell). Once the vector field was calculated they were first masked to only
508 include displacements in regions where there were cells, and filtered to remove outliers. All
509 vectors outside of the masked region were set to zero. Vectors that had a magnitude of greater
510 than 30 pixels/frame (1.1 μm/min) or a signal-to-noise correlation ratio of less than 1.035 were

511 considered outliers. These vectors were removed and replaced with a vector representing the
512 local mean of the surrounding vectors with a kernel size of 3 pixels.

513

514 Once displacement fields were measured, we performed additional analyses to determine the
515 average magnitude and direction of the velocity vectors in each frame over time. The average
516 direction was calculated by determining the cosine of the angle between the displacement
517 vector and a unit vector that points along the x-axis (i.e. towards the open area, cos(θ)). These
518 values were averaged over all vectors in the masked region of the image. To calculate the local
519 correlation of these values within the field, we performed an autocorrelation of the masked
520 vector field with itself (Angelini et al., 2010). The resulting correlation was normalized to 1 and
521 then radially averaged. A correlation length was determined by fitting this curve to a single
522 exponential decay $C(r) = \mathrm{e}^{-r/R_0}$, where R_0 represents the decay length. All analyses were
523 performed in python. Code and example data are available at https://github.com/OakesLab.

524

525 *Epithelial sheet-disruption Assay*

526 Epithelia resistance to mechanical disruption was measured using a "Dispase assay" as
527 previously described (McEwen et al., 2014; Wood et al., 2017). Cells (400,000) were plated on
528 12-well plates (Corning) for 48hr, then washed and pre-incubated for 15mins with calcium-free
529 HBSS + 20mM HEPES. Cell monolayers were lifted from plate wells by incubating at 37°C with
530 a filtered solution of HBSS, 20mM HEPES, 20mg/mL dispase II (Roche), 0.3μM calcium, and
531 0.5μM magnesium. Monolayers were subjected to a shaking force of 1,400 rpm (Thermomixer
532 R, Eppendorf) in 1min increments. Each well was imaged with an iPhone 13 using the 0.5X lens
533 before and after shaking, and the resulting images were analyzed as TIFs in FIJI. Image files
534 were blindly counted for macroscopic fragments using the BlindAnalysisTools plugin, taking the
535 average count from duplicate photos of each well, with 200 serving as the upper limit for
536 fragment counting.

537

538

539 **Key resources Table**

REAGENT or RESOURCE	SOURCE	IDENTIFIER
Antibodies		
Anti-α-catenin	Cell Signaling	Cat#3236
Anti-α-catenin (5B11)		https://www.pnas.org/doi/10.1073/pnas.1308663111
Anti-α-catenin (α18)		Dr. A. Nagafuchi (Nara Medical University, Nara, Japan)
GAPDH	Santa Cruz	Cat# sc-25778
Anti-Vinculin (VIN-11-5)	Sigma	V4505
Anti-Myosin IIA	Sigma	M6064
Anti-phospho-Myosin Light Chain (Thr 18/Ser 19)	Cell Signaling	3674S
Anti-GFP	Invitrogen	A11122
Alexa Fluro 568 phalloidin	Invitrogen	Cat#A12380
Alexa Fluro 488 phalloidin	Invitrogen	Cat#A12379
Goat anti-rabbit Alexa Fluor 488	Invitrogen	Cat#A11008
Goat anti-mouse Alexa Fluor 568	Invitrogen	Cat#A11004
HRP-conjugated goat anti-mouse	BioRad	Cat#1706516
HRP-conjugated goat anti-rabbit	BioRad	Cat#1706515
Donkey anti-mouse	LiCor Biosciences	P/N 925-68072
Donkey anti-rabbit	LiCor Biosciences	P/N: 926-32213
Chemicals, Peptides, and Recombinant Proteins		
Hoechst 33342	ThermoFisher Scientific	Cat#62249
ProLong Gold Antifade Mountant	ThermoFisher Scientific	Cat#P36934
Dispase	Roche	Cat#04942078001
TransIT-2000	Mirus	Cat#MIR-5400
Lipofectamine RNAiMax	Invitrogen	Cat#13778-150
PureYield Plasmid Midiprep System	Promega	Cat#A2492
Mitomycin	Sigma-Aldrich	Cat#M5353
Critical Commercial Assays		

Experimental Models: Organisms/Strains		
Madin-Darby canine kidney II cells	Gumbiner Lab (1996)	Heidelberg strain (Kai Simmons Lab)
Software and Algorithms		
FIJI/ImageJ (version: 2.1.0/1.53c)	Schneider, CA et al., 2012	https://imagej.nih.gov/ij/
Stardist FIJI update site	Schmit, U et al., 2018	Cell/nuclear size quantification https://arxiv.org/abs/1806.03535
MTrackJ in ImageScience FIJI update site	Meijering, E et al., 2012	https://imagej.net/plugins/mtrackj
Blind Analysis Tools FIJI update site	Jaiswal, A and Lorenz, Holger, 2019.	https://imagej.net/plugins/blind-analysis-tools
OpenPIV	Liberzon, A et al., 2021.	PIV package for python https://github.com/OpenPIV/openpiv-python
Graphpad Prism		https://www.graphpad.com/scientific-software/prism/
Github MDCK PIV analysis	Oakes Lab	https://github.com/OakesLab/MDCK_PIV_Analysis/tree/main
Other		
BioStation IM-Q Live Imaging Microscope	Nikon Instruments	
Axioplan2 Epifluorescence Microscope	Zeiss	AxioCAM HR Camera, AxioVision 4.8 software, 20x air objective
A1R Laser Scanning Confocal Microscope	Nikon Instruments	Laser Point Scanning, GaAsP detectors, Plan-Apochromat 60x/1.4 objective
Ti2 Brightfield Microscope	Nikon Instruments	Wide-field Nikon DS-Qi2 Camera, Tokai Hit live cell stage top system, 20X air objective.
Plasmids		
αE-catenin-monomeric RFP in pcDNA3.1	Invitrogen	Ishiyama et al., 2018
αE-catenin-monomeric GFP in modified pCAN	Modified pCAN vector (Ichii & Takeichi, 2007)	Ishiyama et al., 2018; eGFP with the dimerization-disrupting A206K mutation (Zacharias et al., 2002)).

Monomeric GFP-αE-catenin	VectorBuilder	Human α-Ecat sequence/*CTNNA1*
Monomeric GFP-αE-catenin H0-FABD+	VectorBuilder	$R_{666}AIM_{669}$ → GSGS
Monomeric GFP-αE-catenin M-Open-KRR	VectorBuilder	$K_{525}R_{548}R_{551}$ → AAA
Monomeric GFP-αE-catenin M-Open-DDD	VectorBuilder	$D_{392}D_{500}D_{503}$ → AAA

540

541 **FIGURE LEGENDS**
542

543 **Figure 1: An α-cat actin-binding domain unfolding mutant with enhanced binding to**
544 **actin filaments increases cell-cell adhesive strength in MDCK cells.** (**A**) Generation of α-
545 cat knock-out MDCK cells via CRISPR-Cas9. Schematic shows location of guide RNAs
546 (gRNA.5 and gRNA.2) targeting the MTSVHTGN translational start site (TSS) protein sequence
547 within exon2 of *CTNNA1* gene. (**B**) Immunoblot characterization of clonally expanded α-catenin
548 knock-out lines 5.1, 5.2, 2.1 and 2.2 from gRNA.5 or gRNA2, respectively. Note that gRNA5 led
549 to clones robustly expressing an α-cat fragment (*) likely generated by an alternative
550 translational start site (Bullions et al., 1997). We chose to restore wild-type (WT) α-cat and
551 mutant using α-cat KO clone 2.2. MDCK-parental cell line shown as control (clone 2.2* denotes
552 clone used for reconstitution in this study). (**C**) Immunoblot of MDCK KO2.2 cells transfected
553 with RFP or GFP-tagged versions of WT α-cat or an F-actin-binding-domain (FABD) unfolding
554 mutant (α-cat-H0-FABD$^+$). GAPDH was used as loading control. (**D**) Schematic shows location
555 of force-sensitive Helix 0 (H0) in the α-cat actin-binding domain and the H0 unfolding mutant.
556 (**E**) Epithelial sheet disruption assay of MDCK KO2.2 cells expressing WT α-cat (top) or α-cat-
557 H0-FABD$^+$ (bottom). Representative monolayers after mechanical stress treatment under a
558 gradient of calcium concentrations (to sensitize calcium-sensitive, cadherin homophilic binding
559 activity) are shown. (**F**) Quantification of monolayer fragments after mechanical disruption using
560 an orbital shaker. Error bars show mean ± SD (n=3, technical replicates), ****$p<0.0001$, paired t-
561 test.

562

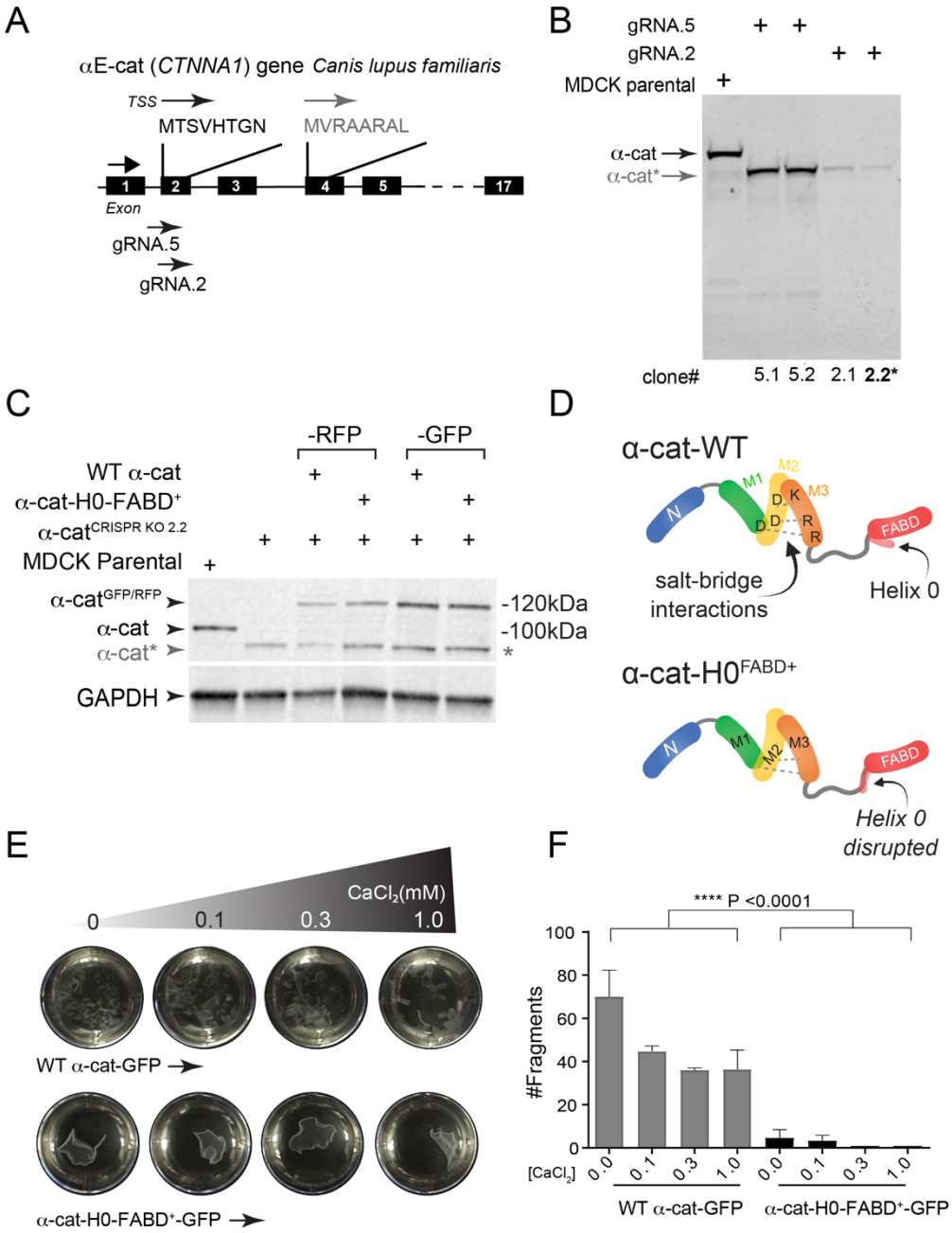
A
αE-cat (CTNNA1) gene Canis lupus familiaris
TSS
MTSVHTGN
MVRAARAL
1
2
3
4
5
17
Exon
gRNA.5
gRNA.2
B
gRNA.5
gRNA.2
MDCK parental
α-cat
α-cat*
clone#
5.1 5.2 2.1 2.2*
C
-RFP
-GFP
WT α-cat
α-cat-H0-FABD+
α-catCRISPR KO 2.2
MDCK Parental
α-catGFP/RFP
α-cat
α-cat*
GAPDH
-120kDa
-100kDa
*
D
α-cat-WT
N
M1
M2
M3
FABD
salt-bridge interactions
Helix 0
α-cat-H0FABD+
Helix 0 disrupted
E
CaCl2(mM)
0
0.1
0.3
1.0
WT α-cat-GFP
α-cat-H0-FABD+-GFP
F
**** P <0.0001
#Fragments
[CaCl2]
WT α-cat-GFP
α-cat-H0-FABD+-GFP

563

564

565 **Figure S1: Characterization of α-cat CRISPR-KO 2.2 MDCK cells.** (**A**) Immunofluorescence
566 confocal image analysis of parental MDCK cells (top row), α-cat CRISPR-KO 2.2 MDCK cells
567 (middle row) and GFP-α-cat-restored α-cat CRISPR-KO 2.2 MDCK cells (bottom row) stained
568 for α-cat (green), F-actin (magenta) or DNA (gray). En face images are shown as maximum z-
569 projections with x-z optical sections to right. White arrowhead shows localization of optical z-
570 section. Scale is 10μm. Note α-cat short isoform expression in CRISPR-KO 2.2 MDCK cells
571 (Fig. 1B) shows no clear localization to cell-cell contacts**.** (**B**) Graph shows quantification of
572 MDCK monolayer adhesive strength after Dispase-treatment and mechanical shaking (as in Fig.
573 1E-F). Note wild-type α-cat-GFP-restored CRISPR-KO 2.2 MDCK cells rescue monolayer
574 integrity to a similar extent as parental MDCK cells.

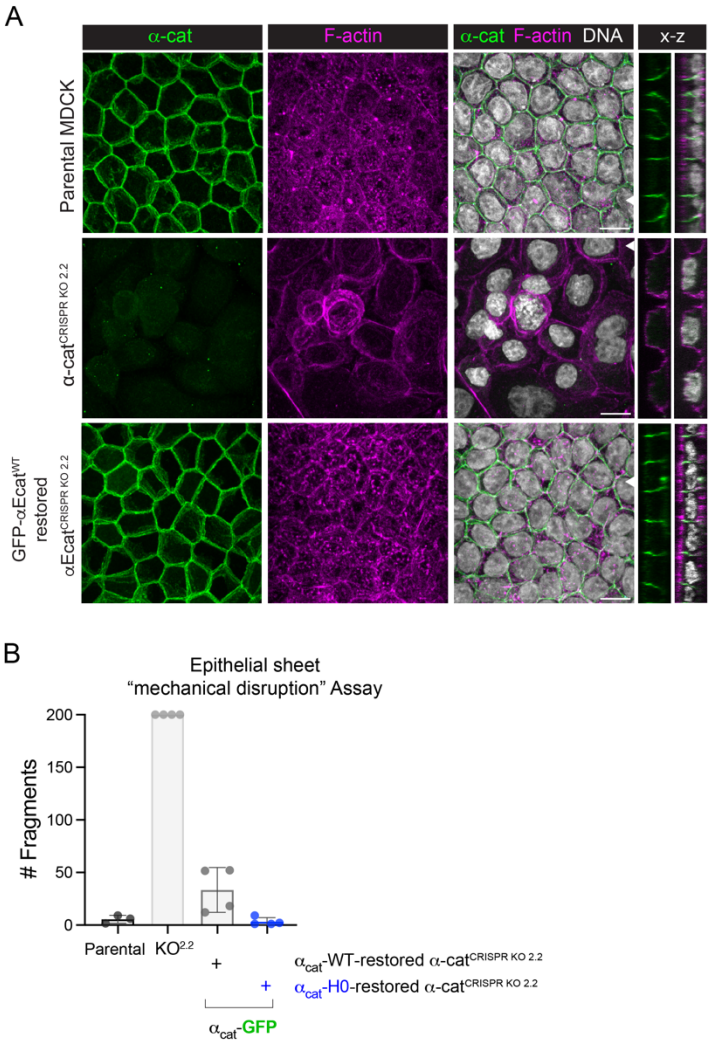

575

576 **Figure 2: α-cat-H0-FABD$^+$ enhances colocalization with F-actin in MDCK cells.**

577 (**A**) WT α-cat-RFP and α-cat-H0-FABD$^+$-RFP MDCK monolayers (10-12 days on Transwell
578 0.4μm filters) were stained for phalloidin. Confocal (x-y) and representative x-z orthogonal
579 images (white arrowhead denotes section line) are shown. Bars, 10μm. (**B**) Intensity profiles of
580 α-cat-RFP and F-actin along bicellular junctions (yellow lines in A). (**C**) Colocalization analysis
581 of α-cat-RFP and F-actin (junctions in A). Each symbol represents the normalized intensity
582 (n.a.f.u.) of α-cat and F-actin at 0.1μm junctional ROIs (n=80). Intensity correlation was
583 analyzed by Pearson's (WT r = -0.536; H0 r = 0.444; ****p < 0.0001) and linear fit plotted with
584 95% CI (WT slope = -0.488 [-0.662 to -0.315]; H0 slope = 0.482 [0.263 to 0.701]). (**D**) WT α-
585 cat-RFP and α-cat-H0-FABD$^+$-GFP were co-cultured and stained for phalloidin (phalloidin
586 shown in grayscale). The inverse correlation between WT α-cat and actin appears most
587 prominent for the C-terminally tagged α-cat lines, which were selected for higher protein
588 expression levels (Fig. S3); we cannot rule-out tag placement as co-contributing to this
589 distribution. Representative x-z orthogonal images are shown. Bar, 10μm. Note α-cat-H0-
590 FABD$^+$expression is not associated with elevated levels of F-actin at cell-cell junctions.

591

592

593

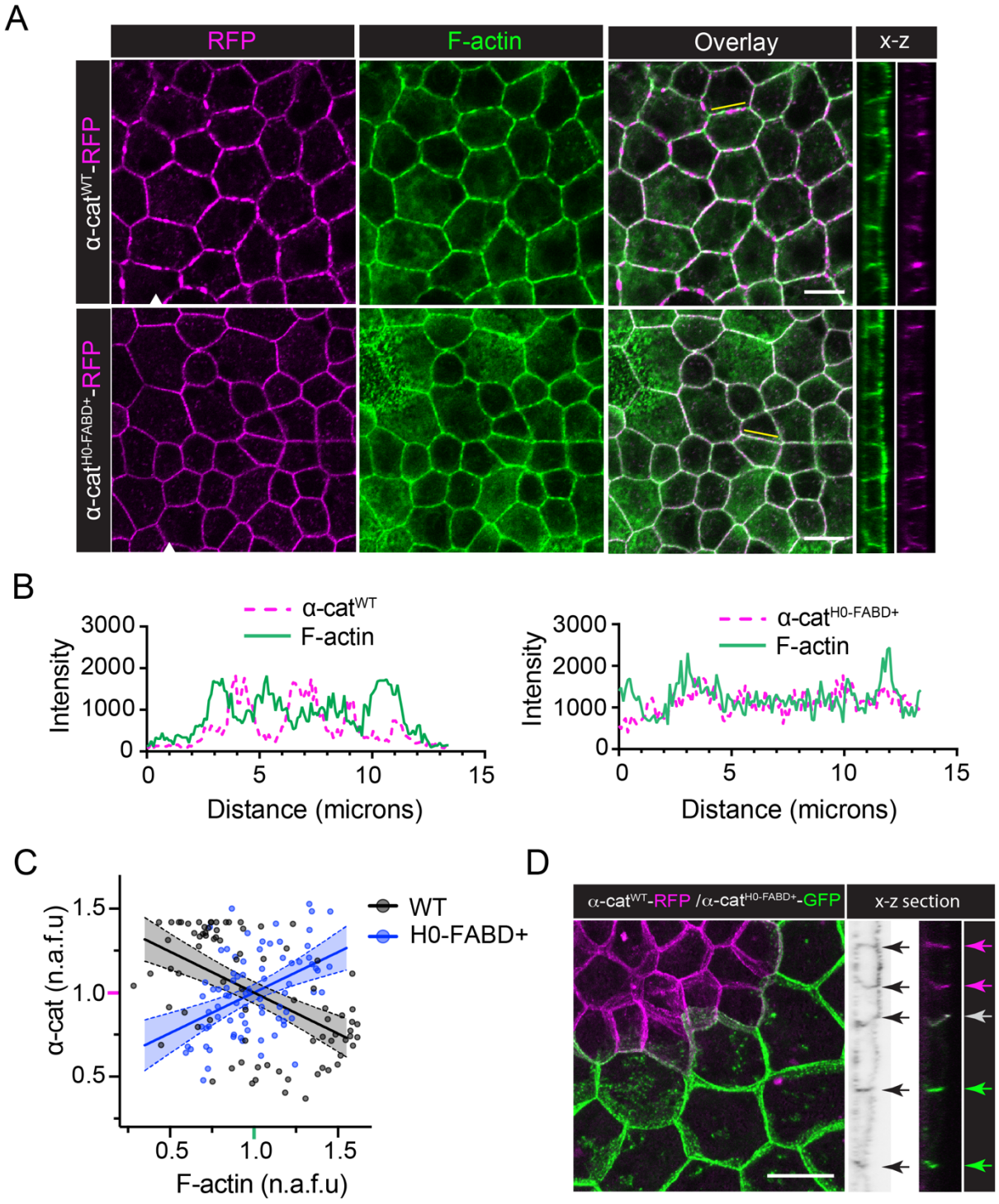
A
RFP
F-actin
Overlay
x-z
α-catWT-RFP
α-catH0-FABD+-RFP
B
α-catWT
F-actin
Intensity
3000
2000
1000
0
0
5
10
15
Distance (microns)
α-catH0-FABD+
F-actin
Intensity
3000
2000
1000
0
0
5
10
15
Distance (microns)
C
α-cat (n.a.f.u)
1.5
1.0
0.5
0.5
1.0
1.5
F-actin (n.a.f.u)
WT
H0-FABD+
D
α-catWT-RFP /α-catH0-FABD+-GFP
x-z section

594

595 **Figure 3: α-cat M2-domain α-18 epitope and vinculin recruitment are similarly accessible**
596 **to α-cat-H0-FABD$^+$ and WT-α-cat.** (**A, B**) α-cat M2-domain α-18 epitope shows no preference
597 for α-cat-H0-FABD$^+$ over WT-α-cat. WT α-cat-RFP (magenta) and α-cat-H0-FABD$^+$-GFP
598 (green) were co-cultured on Transwell filters for 10-12 days, fixed and stained with α18
599 monoclonal antibody (grayscale). Representative x-z orthogonal images are shown (white
600 arrowhead shows section line). Insets (i) and (ii) show zoomed-in views (right). Bar, 10μm. Note
601 that while the α18 epitope is more accessible in α-cat-H0-FABD$^+$ (green) cells in A (x-z
602 grayscale image), B shows the α18 epitope is more accessible in α-cat-WT (magenta) cells. (**C**)
603 Confocal image of filter-grown WT α-cat-GFP and α-cat-H0-FABD$^+$-GFP MDCK cells fixed and
604 stained for vinculin (magenta). En face image taken from apical-most plane. Arrows (white)
605 show similarly modest enrichment of vinculin at apical junctions. Bar, 5μm (**D**) Quantification of
606 junctional vinculin enrichment, with each symbol representing the intensity ratio between paired
607 junction (BCJ) and cytoplasm (Cyto) 1μm ROIs (n = 50). Vinculin localization was not affected,
608 as determined by t test p = 0.966.

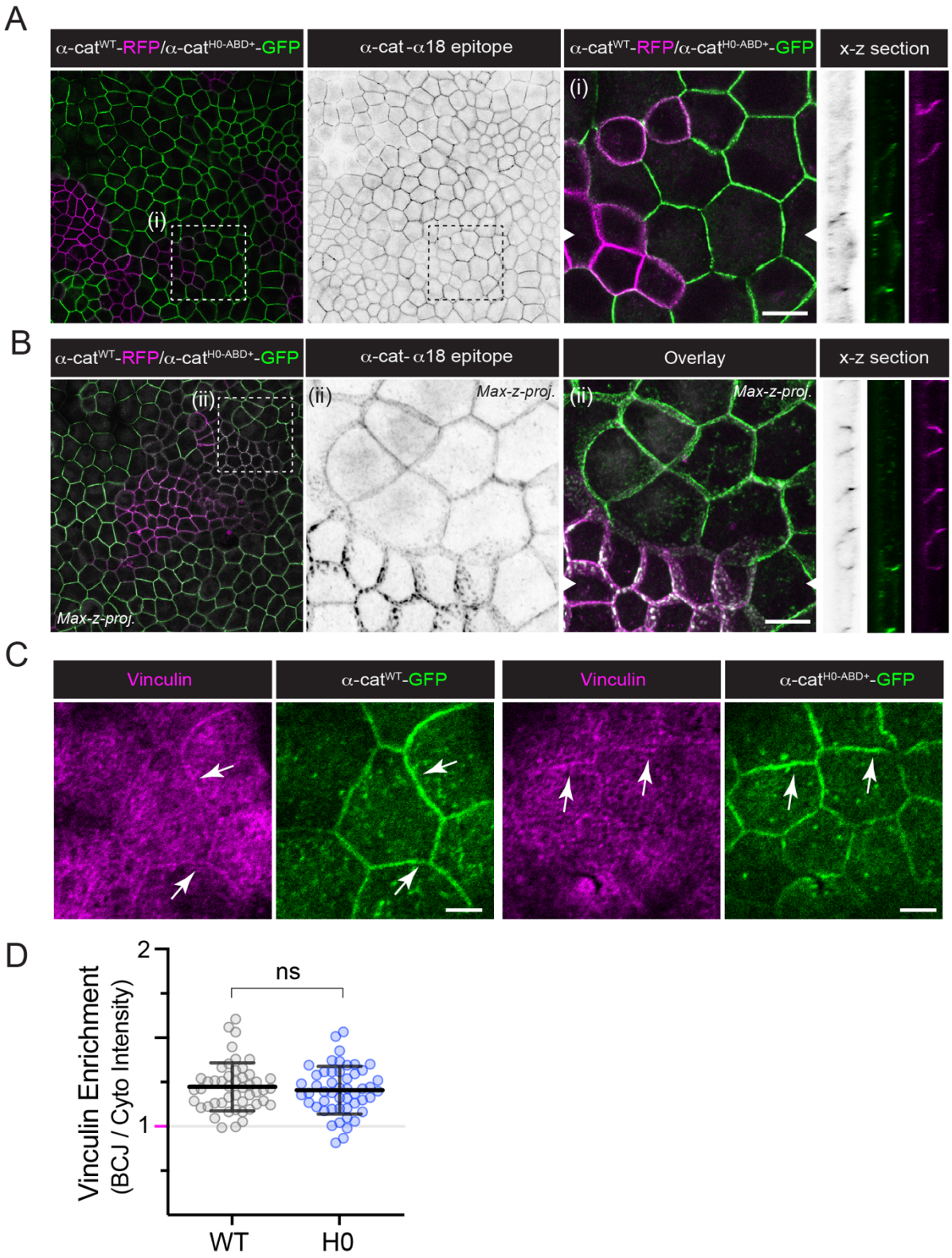
A
α-cat^WT-RFP/α-cat^H0-ABD+-GFP
α-cat-α18 epitope
α-cat^WT-RFP/α-cat^H0-ABD+-GFP
x-z section
(i)
(i)
B
α-cat^WT-RFP/α-cat^H0-ABD+-GFP
α-cat-α18 epitope
Overlay
x-z section
(ii)
(ii)
(ii)
Max-z-proj.
Max-z-proj.
Max-z-proj.
C
Vinculin
α-cat^WT-GFP
Vinculin
α-cat^H0-ABD+-GFP
D
Vinculin Enrichment
(BCJ / Cyto Intensity)
2
1
ns
WT
H0

609

610

611 **Figure 4: α-cat-H0-FABD⁺ interferes with normal packing of MDCK cells.**

612 (**A**) WT α-cat-RFP and α-cat-H0-FABD⁺-RFP -expressing MDCK monolayers (matured 12 days
613 on Transwell 0.4μm filters, magenta) were fixed and stained with phalloidin (green). Magenta
614 asterisk indicates cells with extra small apical area; white asterisk indicates cells with extra-large
615 area. Bar, 10μm. (**B**) Cell number distributions of apical areas in WT α-cat-RFP and α-cat-H0-
616 FABD⁺-RFP cells. Data from three independent FOVs using FIJI-StarDist plug-in. (**C**) Violin plot
617 of apical areas in WT α-cat-RFP and α-cat-H0-FABD⁺-RFP cells. Mean apical areas are not
618 significantly different by unpaired t-test, but the distribution of apical areas (**B**) is significantly
619 different by Kolmogrov-Smirnov analysis (****$p < 0.0001$). This cell-packing phenotype is
620 strongest for our C-terminally tagged α-cat lines, which also show higher protein expression
621 levels (Fig. S3).

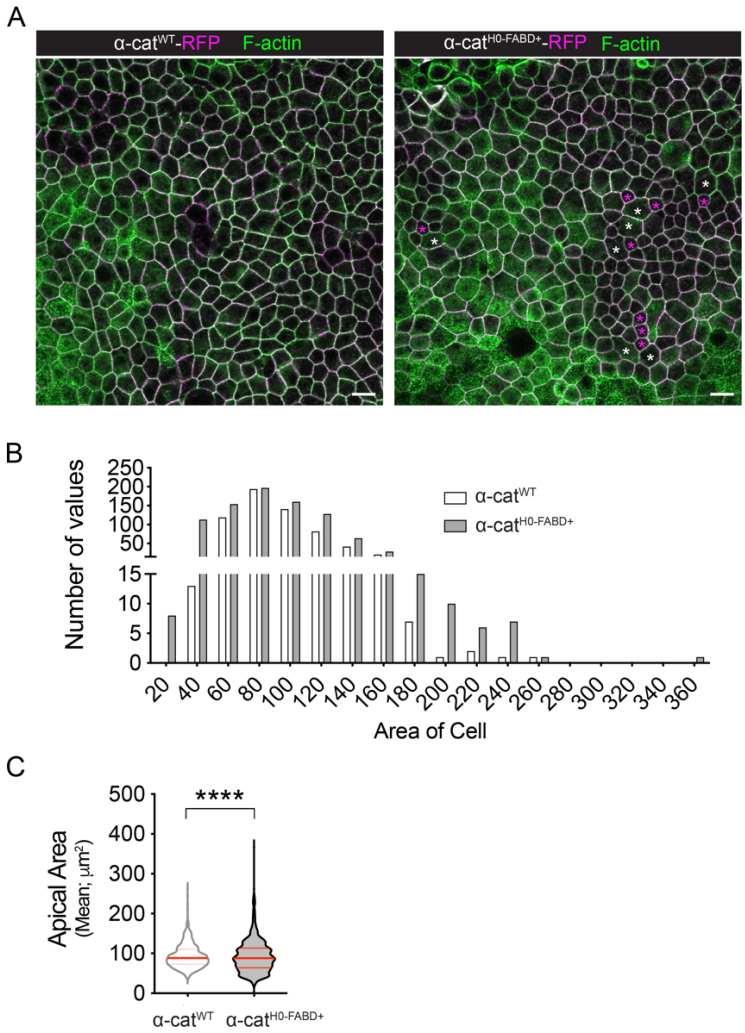

622

Figure 5: α-cat-H0-FABD⁺ slows MDCK epithelial sheet wound closure.

(**A**) Scratch wound healing assays with MDCK KO2.2 cells restored with WT α-cat-GFP or α-cat-H0-FABD⁺-GFP. GFP signals at wound front area at 0-hr or 8-hr are shown. Zoom-in views (i and ii) show "finger-like" protrusions (green arrows). (**B**) Dot distribution plot showing wound closure area covered by WT α-cat-GFP or α-cat-H0-FABD⁺-GFP after 8hrs. Data from three independent repeats, mean ±SD. ****p<0.0001 by ANOVA. (**C**) Representative plot traces showing faster migration rate of WT α-cat-GFP versus α-cat-H0-FABD⁺-GFP cells throughout an entire time-course. (D) Graph showing reduced persistence of α-cat-H0-FABD⁺ cells at wound front compared with WT α-cat cells. Persistence (net displacement/individual cell path length) was quantified using the MTrack FIJI plug-in. Data are presented as mean ±SD with significance by Student t-test * p<0.05.

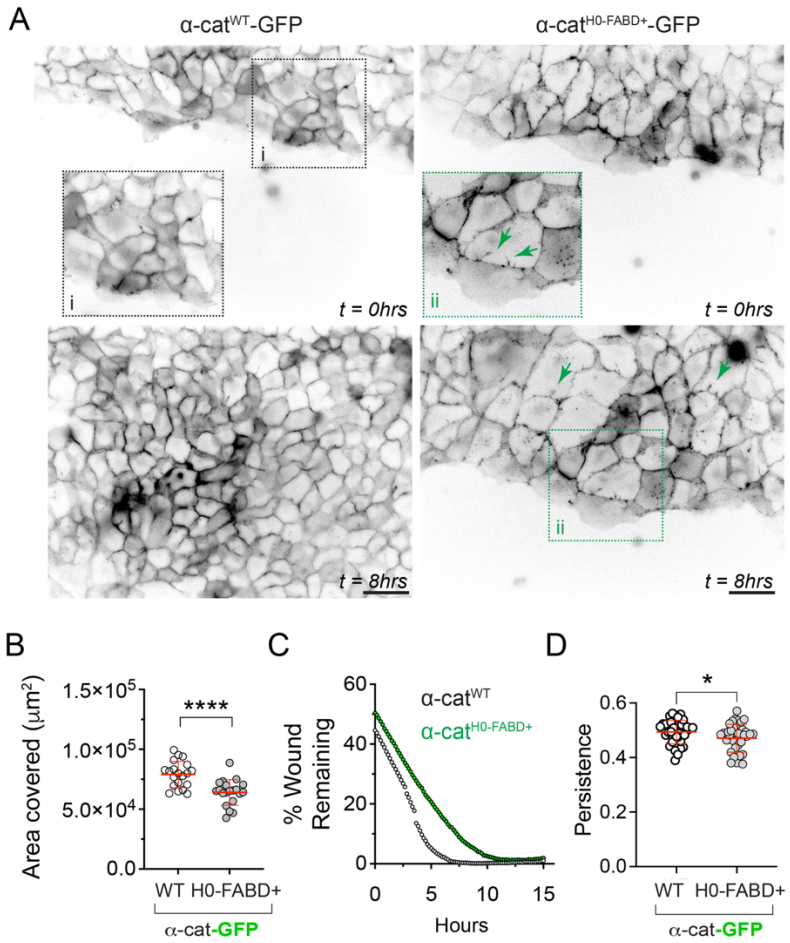

636 **Figure S2: Finger-like tubular invaginations form equally between WT α-cat and α-cat-H0-**
637 **FABD⁺ expressing MDCK wound front leader and follower cells.**

638 *Supplemental images to Figure 5* **(A)** Time-lapse images of MDCK KO2.2 cells restored with
639 WT α-cat-GFP or α-cat-H0-FABD⁺-GFP. Native GFP fluorescence shown in grayscale
640 (inverted). Cyan arrows point to finger-like invaginations at interface between leader cell and
641 follower cell. (**B-D**) Quantification of tubular invaginations (n = 51 for WT α-cat and 46 for α-cat-
642 H0-FABD⁺: (**B**) Length, unpaired t-test, p = 0.4101; (**C**) Fluorescence intensity, unpaired t-test, p
643 = 0.3477; (**D**) Direction/angle formed by tubular invagination and direction of sheet migration,
644 Kolmogorov-Smirnov test, where asterisk (*) reflects p = 0.0408. (**E**) Representative WT-α-cat
645 tubular invaginations (cyan arrows) align with direction of migration (phase image, colored
646 tracks); α-cat-H0-FABD⁺ invaginations align perpendicular to direction of migration. Scale bar,
647 5μm.

648

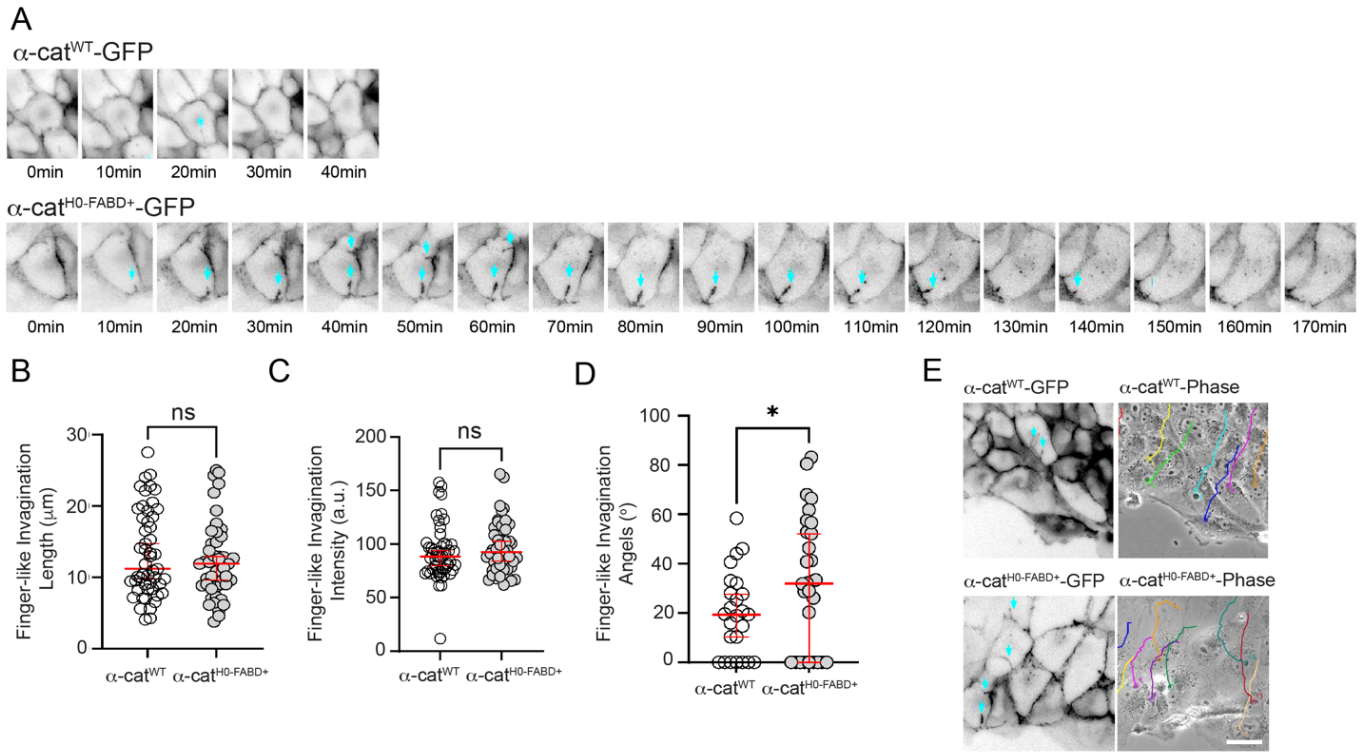

649

650 **Figure 6: α-cat-Middle domain salt-bridge unfolding mutants perturb epithelial cohesion**
651 **and sheet migration more than the α-cat-H0-FABD^{+} 'catch-bond' mutant**.

652 (**A**) Migration capacity of α-cat-WT and α-cat-H0-restored MDCK cells after barrier-removal. Y-
653 axis shows area-covered after 16hrs. N- and C-terminal GFP-tagged versions of α-cat
654 constructs are directly compared. Each symbol reflects a field-of-view quantification. Distinct
655 symbols show biological replicates (n = 4) of barrier-release assays from different days. Note
656 the α-cat-H0-FABD^{+} mutant migrates consistently less than α-cat-WT with p values by ANOVA
657 shown. Data are presented as mean ±SD. Asterisks * p = 0.0218 and ** p = 0.0053. Largest
658 differences in migration rate are due to α-cat expression differences more than GFP-tag
659 placement (immunoblot in Fig. S3A). (**B**) Migration capacity of GFP-tagged α-cat-WT, α-cat-H0-
660 FABD^{+}, α-cat-M^{OpenKRR} and α-cat-M^{OpenDDD} -restored MDCK cells after barrier-removal.
661 Corresponding immunoblot in Fig. S3A. Each symbol reflects a field-of-view quantification.
662 Distinct symbols show biological replicates (n= 4) of barrier-release assays from different days.
663 Note the α-cat-M^{OpenDDD} mutant migrates significantly slower than α-cat-WT by ANOVA, where
664 ** for 30,000 cell plating p = 0.005 and ** for 60,000 cell plating p = 0.0097). These relative
665 differences in migration do not simply correlate with epithelial sheet strength quantified in (C).
666 (**C**) Monolayer adhesive strength after mechanical disruption. Y-axis quantifies the number of
667 epithelial fragments after Dispase treatment and mechanical shaking. Each symbol reflects
668 measurements from technical replicates (different wells); distinct symbols show biological
669 replicates (n = 3) from assays on a different day with significance by ANOVA, where **** =
670 <0.0001, *** = 0.0007, * = 0.0328. α-cat WT versus α-cat-M^{OpenDDD} = 0.3468 and α-cat-H0-
671 FABD^{+} versus α-cat-M^{OpenKRR} = 0.0612. Data are presented as mean ±SD.

672

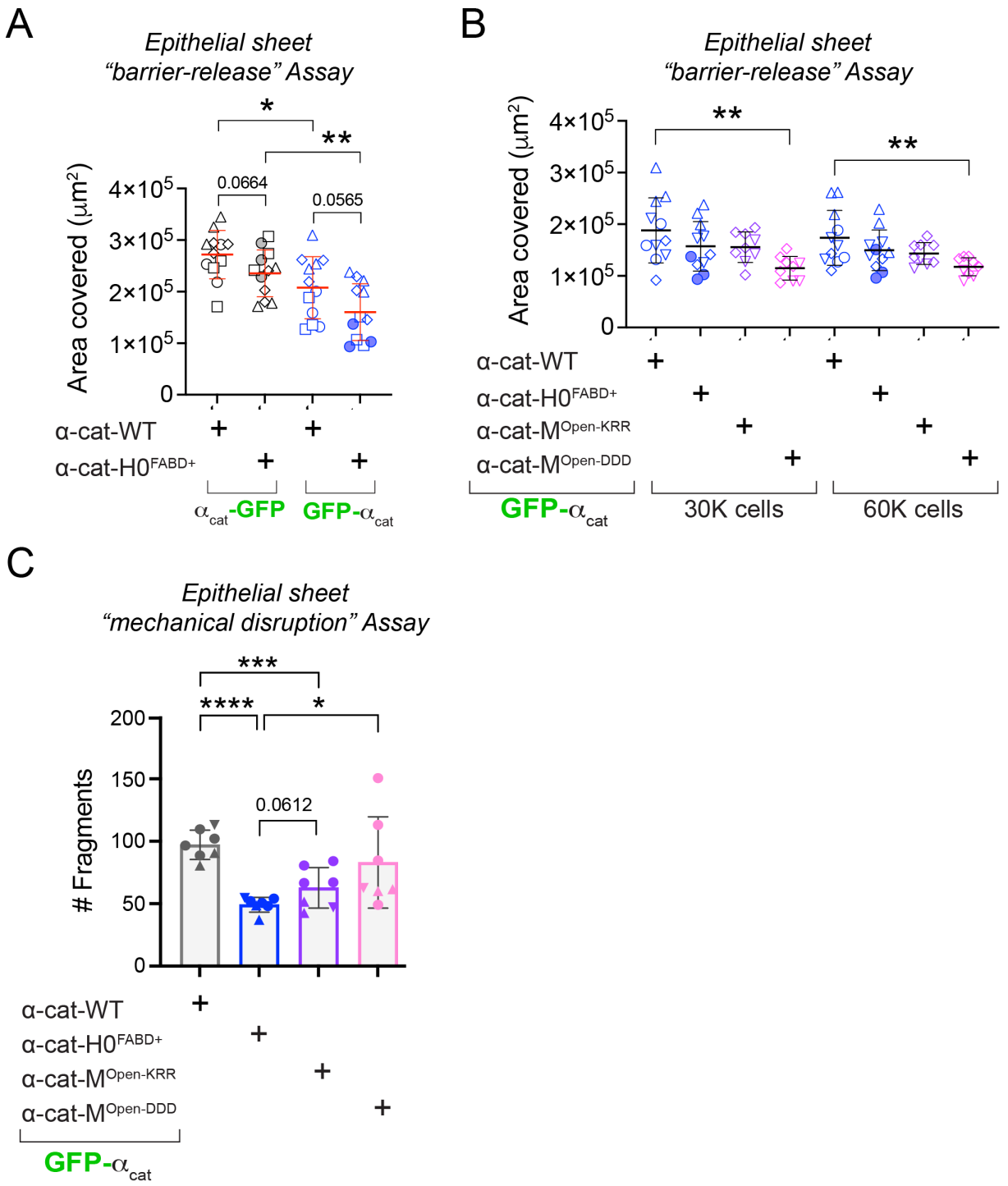
A
Epithelial sheet
"barrier-release" Assay
Area covered (μm²)
4×10⁵
3×10⁵
2×10⁵
1×10⁵
0
*
**
0.0664
0.0565
α-cat-WT
α-cat-H0FABD+
αcat-GFP
GFP-αcat
B
Epithelial sheet
"barrier-release" Assay
Area covered (μm²)
4×10⁵
3×10⁵
2×10⁵
1×10⁵
0
**
**
α-cat-WT
α-cat-H0FABD+
α-cat-MOpen-KRR
α-cat-MOpen-DDD
GFP-αcat
30K cells
60K cells
C
Epithelial sheet
"mechanical disruption" Assay
Fragments
200
150
100
50
0
***
****
*
0.0612
α-cat-WT
α-cat-H0FABD+
α-cat-MOpen-KRR
α-cat-MOpen-DDD
GFP-αcat

673

674 **Figure S3: Characterization of GFP-tagged α-cat cell lines**. (**A**) Immunoblot of N- and C-
675 terminal GFP-tagged α-cat constructs. Vinculin (red) is used as a loading control. Graph shows
676 α-cat protein expression normalized to Vinculin. Data are presented as mean ±SD (n = 3).
677 Higher protein expression of C-terminally tagged α-cat relative to N-terminally tagged α-cat is
678 due to different flow cytometry gating strategies used to select these cell lines. Modest
679 differences in protein expression between GFP-α-cat WT/α-cat-H0-FABD^{+} versus α-cat-M^{Open}
680 constructs are evident, but do not explain differences in epithelial sheet strength or migration
681 seen in Fig. 6. (**B**) Schematic of α-cat-M^{OpenKRR} and α-cat-M^{OpenDDD} constructs, showing location
682 of salt-bridge mutant modified residues. (**C**) Epithelial monolayer adhesive strength assay after
683 mechanical disruption. Y-axis quantifies the number of epithelial fragments remaining after
684 Dispase treatment and mechanical shaking. Each symbol reflects measurements from technical
685 replicates (different wells). The first portion of this graph was shown in Fig. S1. Here we show
686 cohesive strength of N- versus C-terminally tagged α-cat cell lines. Note that parental MDCK
687 cells show strongest intercellular adhesion compared with α-cat CRISPR-KO2.2 cells restored
688 with GFP-tagged-α-catenins. Cells expressing higher levels of α-cat are less prone to
689 fragmentation (see immunoblot in A).

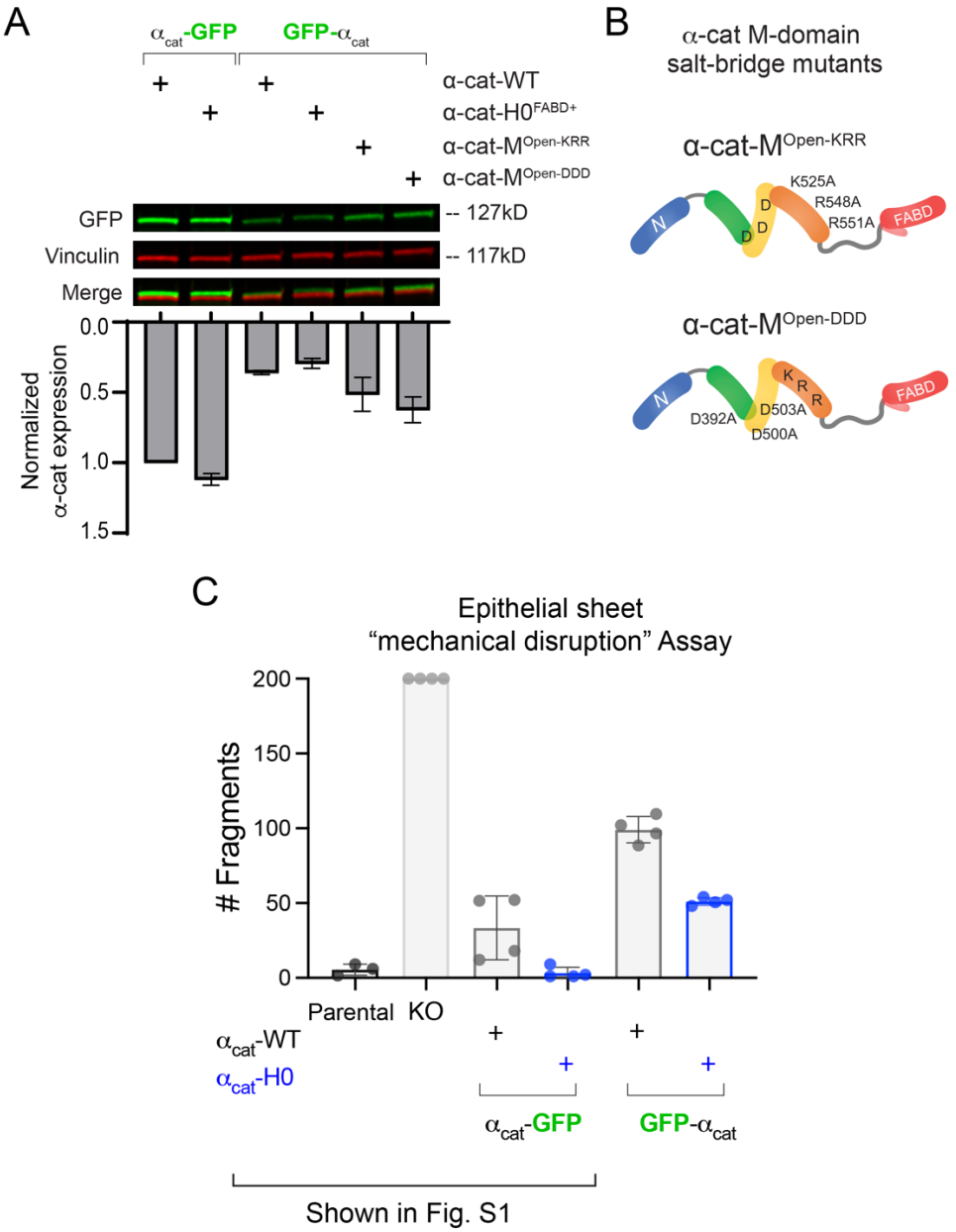
A
αcat-GFP
GFP-αcat
α-cat-WT
α-cat-H0FABD+
α-cat-MOpen-KRR
α-cat-MOpen-DDD
GFP
Vinculin
Merge
-- 127kD
-- 117kD
Normalized α-cat expression
0.0
0.5
1.0
1.5
B
α-cat M-domain salt-bridge mutants
α-cat-MOpen-KRR
K525A
R548A
R551A
FABD
N
D
D
D
α-cat-MOpen-DDD
D392A
D503A
D500A
K
R
R
C
Epithelial sheet "mechanical disruption" Assay
Fragments
200
150
100
50
0
Parental
KO
αcat-WT
αcat-H0
αcat-GFP
GFP-αcat
Shown in Fig. S1

690

691

692 **Figure 7: α-cat-Middle domain salt-bridge unfolding mutants perturb collective**
693 **monolayer speed and coordination more than α-cat-H0-FABD$^+$ 'catch-bond' mutant**. (**A**)
694 Schematic of Particle Image Velocimetry (PIV) analysis of epithelial monolayers. Barrier-release
695 timelapses were background-masked, and calculated flow vectors were analyzed for direction
696 (cos(θ)) and magnitude (velocity). Scale bar = 100μm. (**B**) Average degree of cell-cell
697 coordination during epithelial sheet migration. Y-axis represents the mean cohesive angle,
698 plotted as cos(θ). Data are presented as mean ±SD of 4 biological replicates at initial (t = 0-4 hr)
699 and final (t = 12-16 hr) timepoints, where * = 0.00147 , ** = 0.0040, **** = <0.0001 by ANOVA
700 (Dunnett's multiple comparisons). (**C**) Average velocity of epithelial sheet migration. Data are
701 presented as the mean ±SD of 4 biological replicates at initial and final timepoints, where **** =
702 <0.0001. (**D**) Speed vs. time tracings of monolayers analyzed by PIV. Data are presented as
703 the mean ±SEM of 4 biological replicates with significance by ANOVA, where *** = < 0.0001. (**E**)
704 Spatial correlation of monolayer speed vs time. Data are presented as the mean ±SEM of 4
705 biological replicates with significance by ANOVA, where **** = < 0.0001. α-cat-WT vs α-cat-H0-
706 FABD$^+$ showed no difference in velocity correlation (p = 0.4901), but α-cat-WT showed
707 increased correlation over α-cat-KRR and α-cat-DDD by multiple comparisons (**** = < 0.0001).
708 (**F**) Exponential fit of monolayer velocity correlation as a function of distance (R, μm). α-cat
709 forms show no difference in initial correlation radius, but develop different final correlation radii
710 (*** = 0.0004 by ANOVA); only α-cat-DDD differed by multiple comparisons.

711

712

713

714

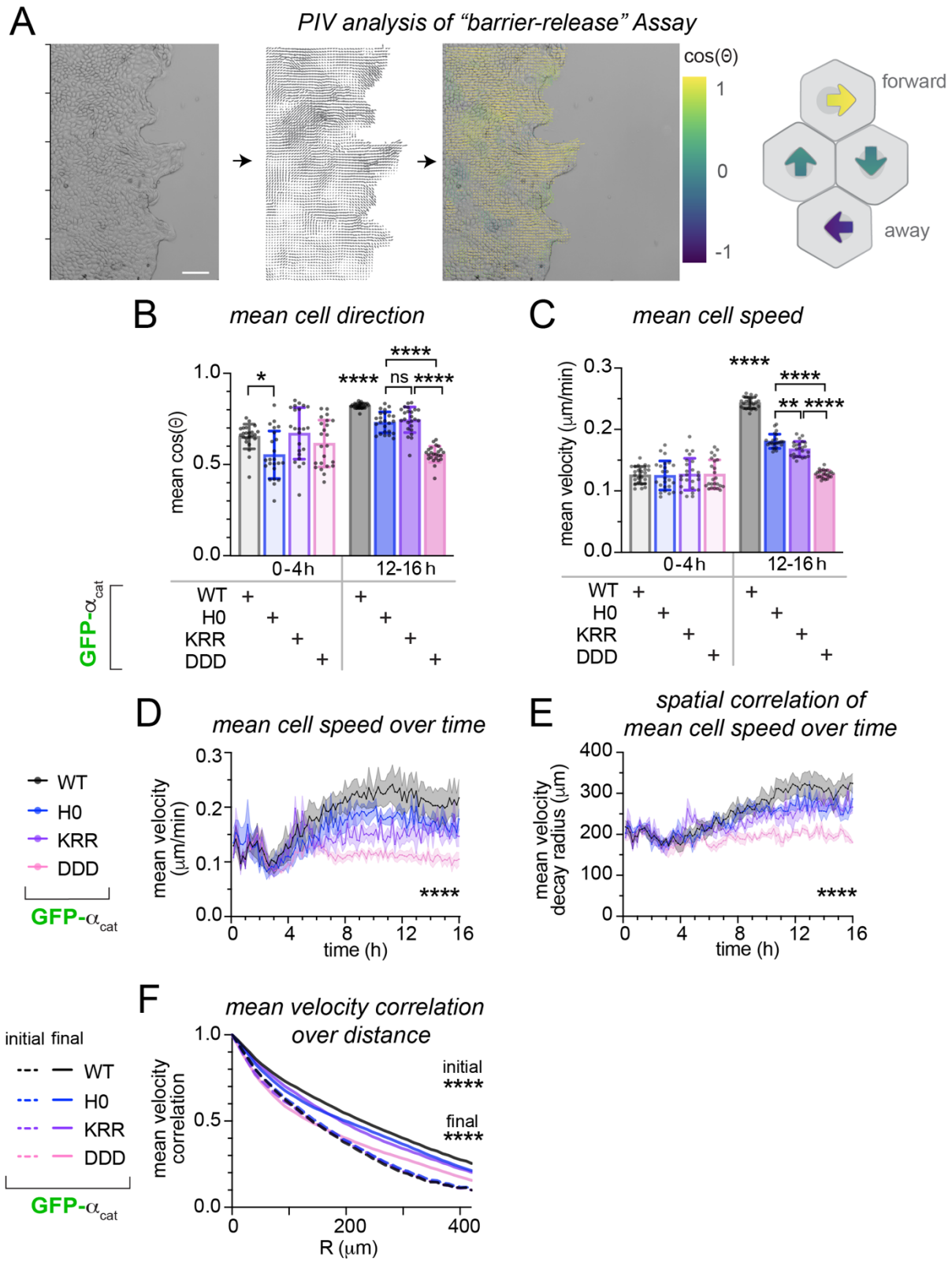
A
PIV analysis of "barrier-release" Assay
cos(Θ)
1
0
-1
forward
away
B
mean cell direction
mean cos(Θ)
1.0
0.5
0.0
*
****
ns
****
****
0-4 h
12-16 h
WT
H0
KRR
DDD
GFP-αcat
C
mean cell speed
mean velocity (μm/min)
0.3
0.2
0.1
0.0
****
****
**
****
0-4 h
12-16 h
WT
H0
KRR
DDD
D
mean cell speed over time
WT
H0
KRR
DDD
GFP-αcat
mean velocity (μm/min)
0.3
0.2
0.1
0.0
****
0
4
8
12
16
time (h)
E
spatial correlation of mean cell speed over time
mean velocity decay radius (μm)
400
300
200
100
0
****
0
4
8
12
16
time (h)
F
mean velocity correlation over distance
initial final
WT
H0
KRR
DDD
GFP-αcat
mean velocity correlation
1.0
0.5
0.0
initial
****
final
****
0
200
400
R (μm)

715

716 **Figure 8: α-cat-M-domain salt-bridge mutants show persistent recruitment of vinculin to**
717 **cell-cell junctions whereas α-cat-WT and α-cat-H0-FABD^{+} do not**. **A**) Immunofluorescence
718 confocal image analysis of α-cat CRISPR-KO 2.2 MDCK cells restored with GFP-α-cat-
719 constructs. Cells grown on glass coverslips were fixed and stained for α-cat (native GFP,
720 green), Vinculin (magenta) and F-actin (cyan). En face images are shown as maximum z-
721 projections. White arrowheads show enhanced recruitment of vinculin to adherens junctions of
722 α-cat-M^{OpenKRR} and α-cat-M^{OpenDDD} constructs relative to GFP-α-cat WT/α-cat-H0-FABD^{+}.
723 Overlay image with insets (dotted boxes) are shown at higher resolution in Fig. S6). Scale is
724 10μm. (**B**) Graph shows junctional vinculin enrichment, with each symbol representing the
725 intensity ratio between paired junction (BCJ) and cytoplasm (Cyto) 1μm ROIs (n = 110+). α-cat
726 constructs affect vinculin localization by ANOVA (**** $p < 0.0001$) with Turkey's multiple
727 comparisons (α-cat WT vs H0-FABD^{+} $p = 0.0920$; α-cat WT vs M^{OpenKRR} and M^{OpenDDD} **** $p <$
728 0.0001).

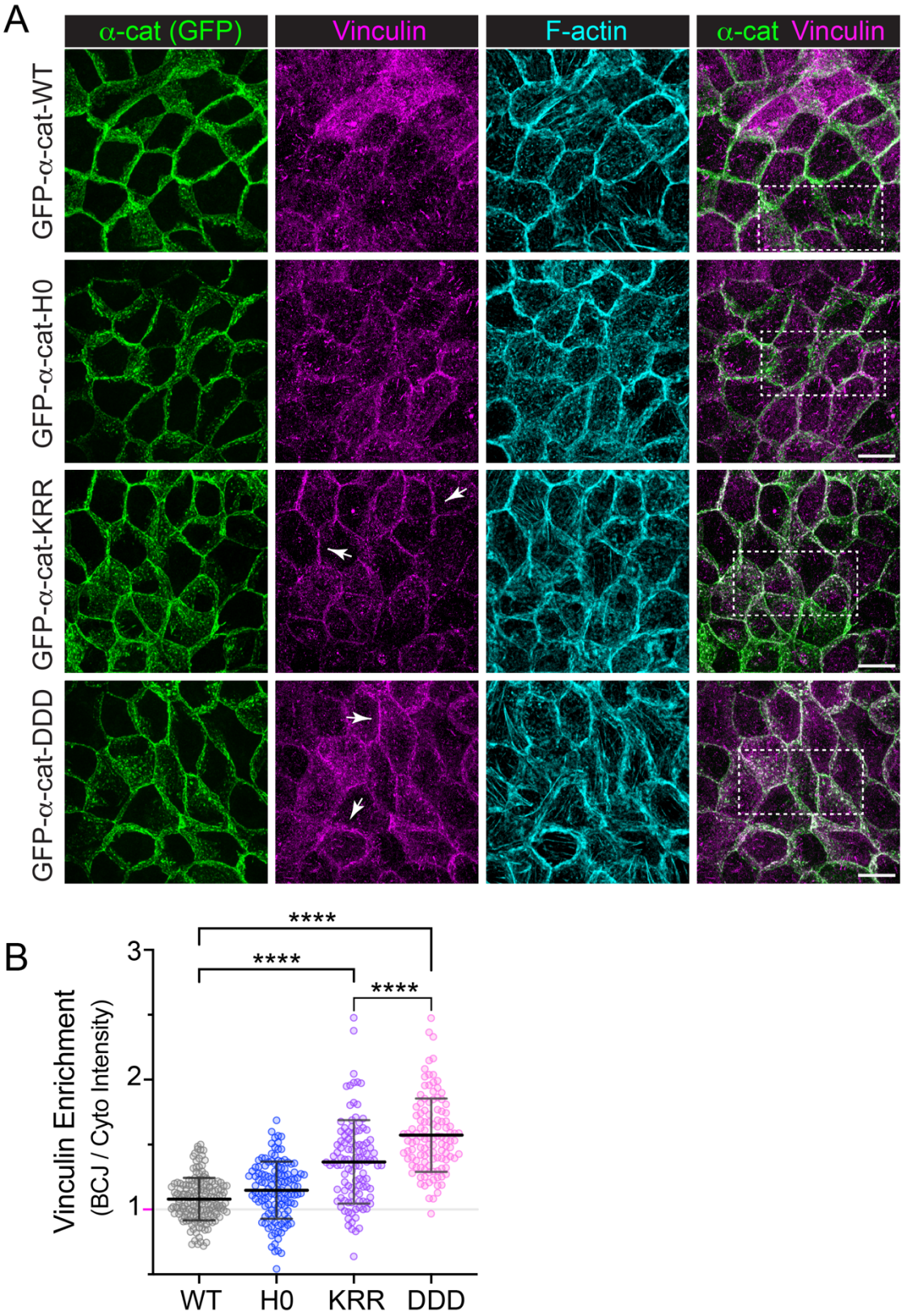
A
α-cat (GFP)
Vinculin
F-actin
α-cat Vinculin
GFP-α-cat-WT
GFP-α-cat-H0
GFP-α-cat-KRR
GFP-α-cat-DDD
B
Vinculin Enrichment
(BCJ / Cyto Intensity)
3
2
1
****
****
****
WT
H0
KRR
DDD

729

730 **Figure S4: Barrier-release epithelial sheet migration assay.**

731 *Supplemental images to Figure 7.* Phase images of GFP-α-cat-restored MDCK cells plated in
732 35mm 4-chambers Ibidi plates (60,000 cells per well). Two hours before imaging, the barrier
733 was pulled, and media was changed to DMEM-10%FBS with 10μg/ml mitomycin C for 2 hours
734 incubation. Media was changed to Fluorobrite media with 10%FBS. Positions were selected
735 along the wound edge and brightfield images were acquired using 20x objective at 10-minute
736 intervals over 16h hours on Ti2 microscope (Nikon). Scale bar = 100μm. Specific cell lines/α-cat
737 constructs are indicated.

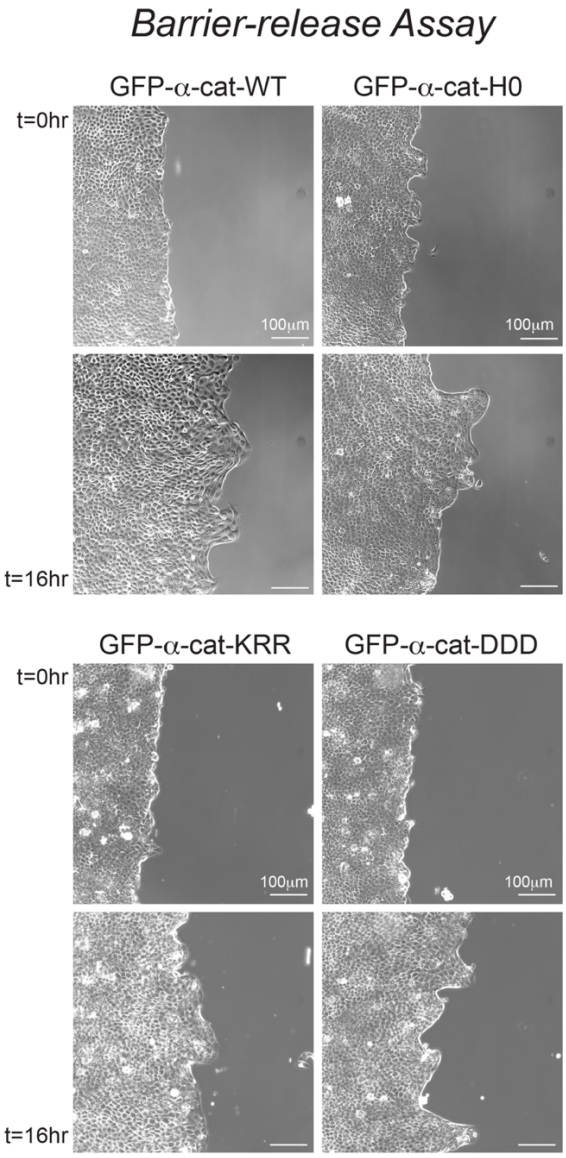

738

739 **Figure S5: α-cat-M-domain salt-bridge mutants show persistent recruitment of vinculin to**
740 **cell-cell junctions compared with α-cat-WT and α-cat-H0-FABD⁺**. *Supplemental images to*
741 *Figure 8.* **A**) Immunofluorescence confocal image analysis of α-cat CRISPR-KO 2.2 MDCK cells
742 restored with GFP-α-cat-constructs. Cells grown on Transwell filter supports for two weeks were
743 fixed and stained for α-cat (native GFP, green), Vinculin (magenta) and F-actin (cyan) (overlay).
744 Individual en face images are shown as maximum z-projections (inverted grayscale). Magenta
745 arrows show enhanced recruitment of vinculin to adherens junctions of α-cat-M^{OpenKRR} and α-
746 cat-M^{OpenDDD} constructs relative to GFP-α-cat WT/α-cat-H0-FABD^{+}. Overlay image with nuclei
747 (gray). Scale is 10μm. (**B**) Inset images from Fig. 8 (dotted boxes) show evidence of α-cat
748 clusters along lateral membranes (cells grown on glass coverslips). Note α-cat cluster size is
749 not obviously different, but co-localization with Vinculin is more clearly evident in α-cat M-
750 domain salt-bridge mutants (white arrows). Scale is 5μm.

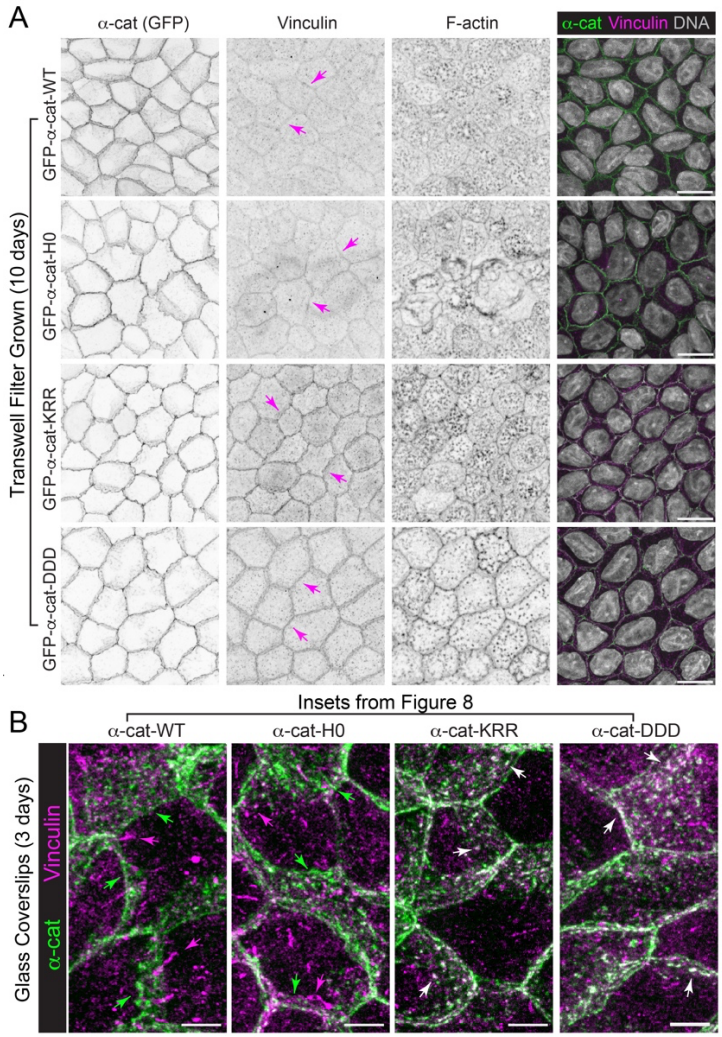

751

752 **Figure 9: α-cat-M-domain salt-bridge mutants show enrichment of phosphorylated-MLC**
753 **to cell-cell junctions compared with α-cat-WT and α-cat-H0-FABD^{+}**.

754 **A**) Immunofluorescence confocal image analysis of α-cat CRISPR-KO 2.2 MDCK cells restored
755 with GFP-α-cat-constructs. Cells grown on Transwell filter supports for two weeks were fixed
756 and stained for α-cat (native GFP, green), ppMLC (magenta) and F-actin (cyan). En face
757 images are shown from a single z-plane. Yellow arrows show enhanced recruitment of ppMLC
758 to adherens junctions of α-cat-M^{OpenKRR} and α-cat-M^{OpenDDD} constructs relative to GFP-α-cat
759 WT/α-cat-H0-FABD^{+}. The apparent gap between basolateral membranes, particularly seen in α-
760 cat -WT and -H0-FABD^{+} images, may be due to monolayers being fixed and stored for over a
761 month before staining. Scale is 10μm. White arrowhead in α-cat/ppMLC overlay images shows
762 where x-z section images are taken and shown in Fig. S6. (**B**) Graph shows quantification of
763 ppMLC junctional enrichment, with each symbol representing the intensity ratio of individual bi-
764 cellular junction (BCJ) points 0.1μm ROIs (n = 160-180) ratioed to fluorescence intensity of the
765 entire field of view. α-cat constructs affect ppMLC localization by ANOVA (**** $p < 0.0001$) with
766 Turkey's multiple comparisons (α-cat WT vs H0-FABD^{+} p = NS; α-cat WT vs M^{OpenKRR} (*p =
767 0.03) and α-cat-H0-FABD^{+} vs M^{OpenKRR} or M^{OpenDDD} p**= 0.0012 and 0.0053, respectively).

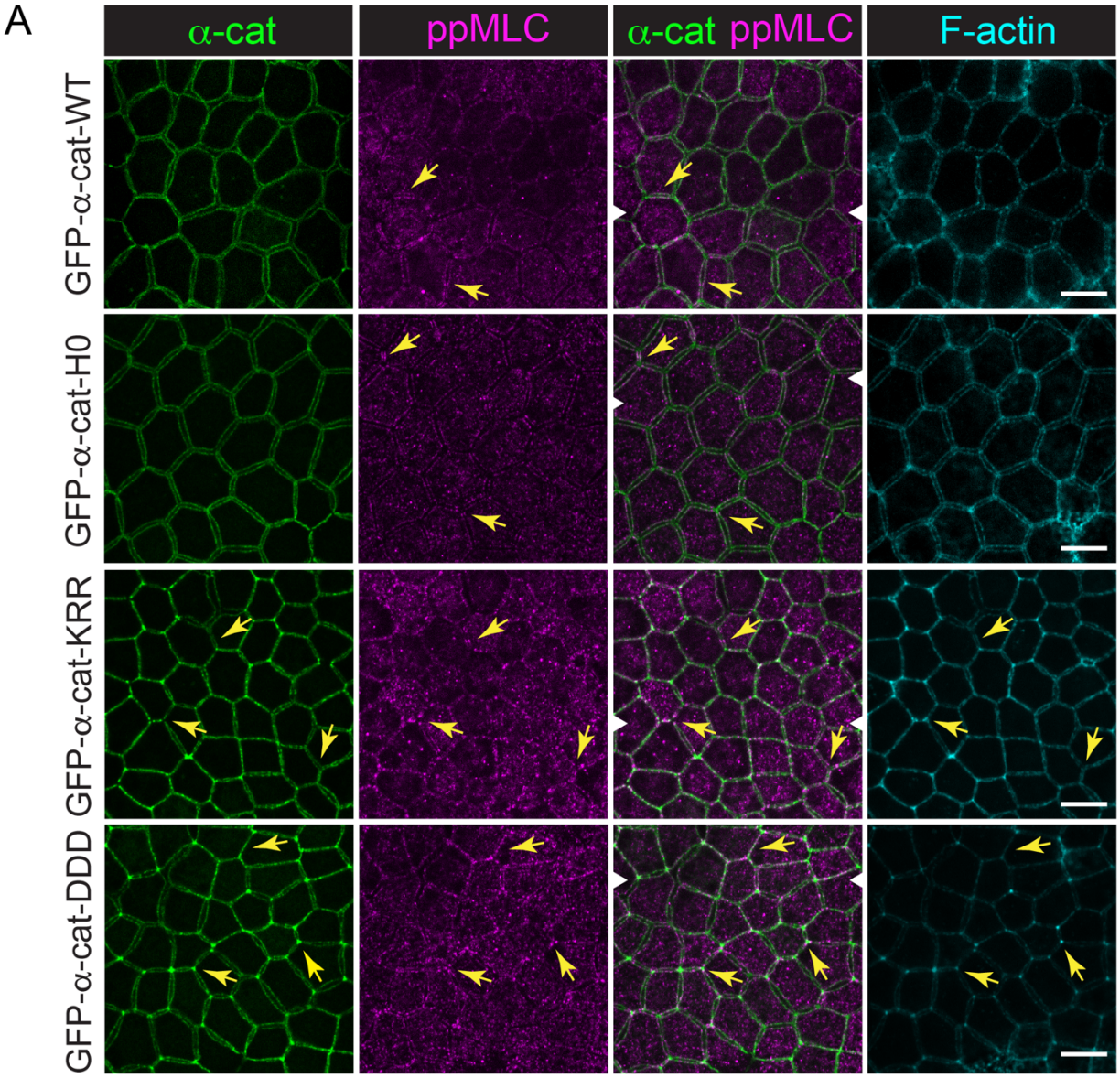
A
α-cat
ppMLC
α-cat ppMLC
F-actin
GFP-α-cat-WT
GFP-α-cat-H0
GFP-α-cat-KRR
GFP-α-cat-DDD

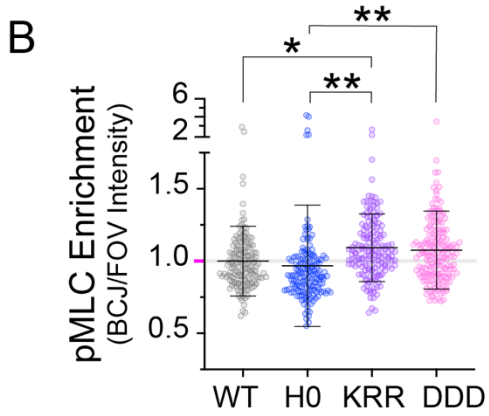
B
pMLC Enrichment
(BCJ/FOV Intensity)
6
2
1.5
1.0
0.5
*
**
**
WT
H0
KRR
DDD

768

769

770 **Figure S6: α-cat-M-domain salt-bridge mutants show enhanced recruitment of phospho-**
771 **Myosin Light Chain (ppMLC) to adherens junctions compared with α-cat-WT and α-cat-**
772 **H0-FABD⁺**. *Supplemental images to Figure 9*. Immunofluorescence confocal image analysis (x-
773 z views) of α-cat CRISPR-KO 2.2 MDCK cells restored with GFP-α-cat-constructs. Cells grown
774 on Transwell filter supports for 1-2 weeks were fixed and stained for α-cat (native GFP, green),
775 ppMLC (magenta) and F-actin (cyan) (overlay). Yellow arrows show enhanced recruitment of
776 ppMLC to adherens junctions of α-cat-M^{OpenKRR} and α-cat-M^{OpenDDD} constructs relative to GFP-α-
777 cat WT/α-cat-H0-FABD^{+}. White arrowheads show z-plane corresponding to x-y images in Figure
778 9. Scale is 10μm.

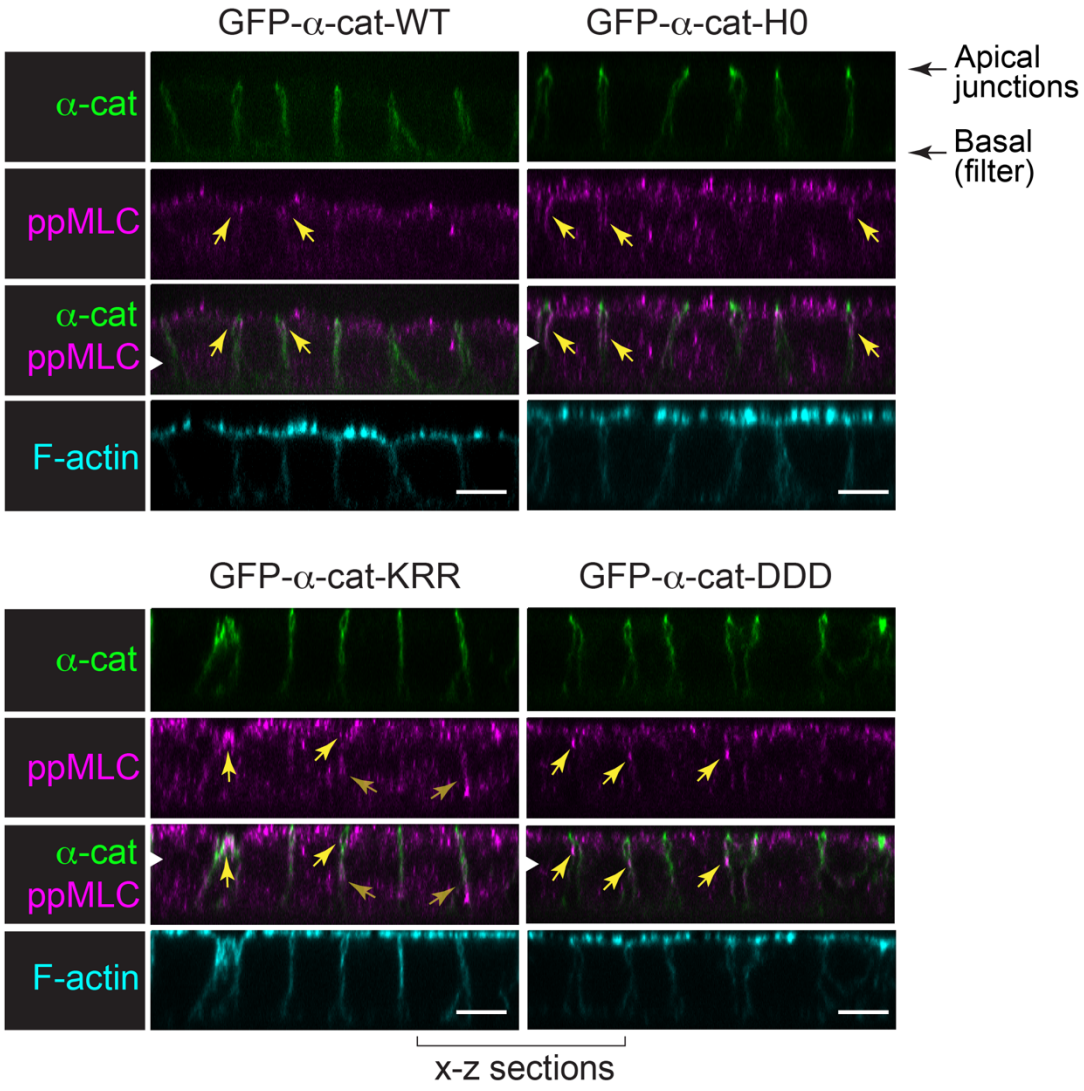

779

780

Figure S7: Schematic of α-cat F-actin-binding domain mutants and properties used in this study. (**Left**) Schematic of WT α-cat actin-binding domain based on crystallographic structure, which reveals bundle of 5 helices and an unstructured C-terminal extension (CTE) (Ishiyama et al., 2018; Ishiyama et al., 2013; Rangarajan and Izard, 2012; Rangarajan and Izard, 2013). WT α-cat shows low affinity binding to F-actin in solution (Actin-pelleting Assay, Kd = 8.5μM) and two-state binding by single molecule force-trap measurements (Buckley et al., 2014; Wang et al., 2022; Xu et al., 2020). (**Middle**) Schematic of α-cat-H0-FABD protein designed by Ishiyama et al (2018) to unfold the short H0-helix. This mutant shows enhanced binding to F-actin in solution (Kd = 2μM). Single molecule force-trap measurements remain untested for this mutant; two-state binding is likely possible based similarity to vinculin. (**Right**) The α-cat-ΔH0-H1-FABD protein of Wang et al (2022) removes both H0-H1 helices. This mutant shows dramatically enhanced (18-fold) binding to F-actin in solution (Kd = 0.5μM) and one-state slip-binding by single molecule force-trap measurements (Wang et al., 2022). Cell based studies carried out here (MDCK cells) and elsewhere (colon carcinoma cell line, Ishiyama, 2018 #1555) suggest the α-cat-H0-FABD mutant is less force-"discriminating" or "selective" of actin filaments than WT α-cat protein, with implications for static versus dynamic cell-cell behaviors. Created with BioRender.

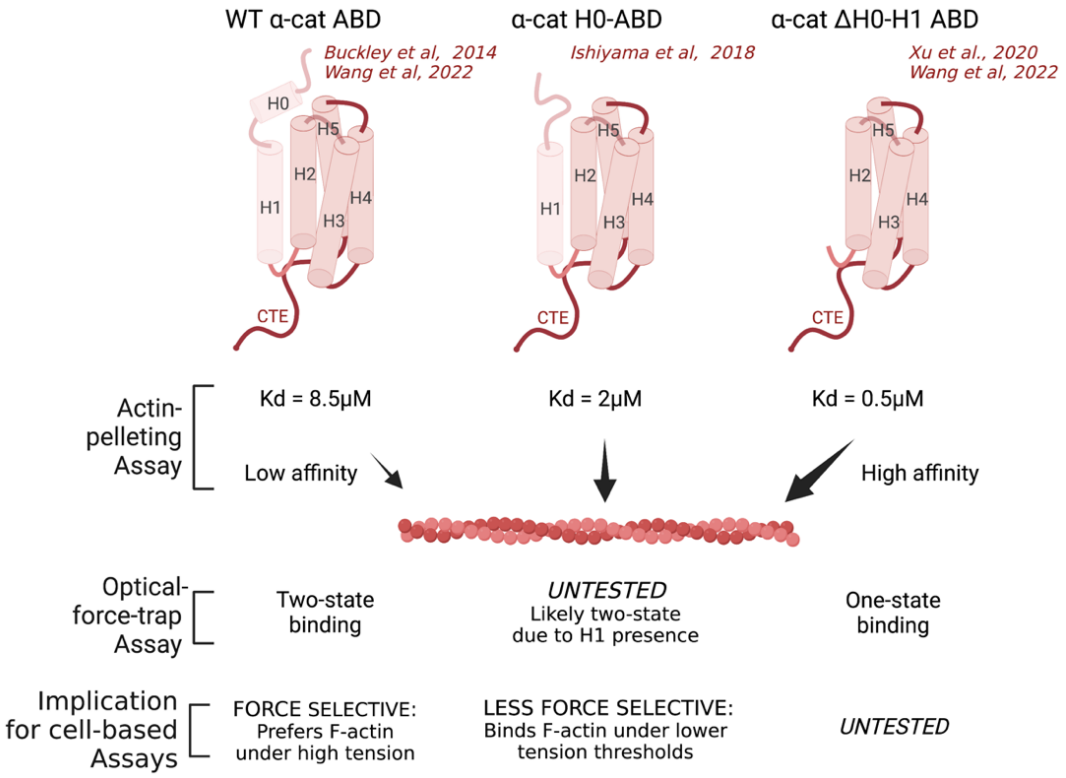

Figure 10: MODEL: Force-desensitized forms of α-cat make distinct contributions to epithelial cohesion, migration and junction organization.

(**A**) Schematic of WT α-cat FABD (red segment of multicolor α-cat protein) binding an actin filament under low tension (left) or high tension (right). "No/weak binding" vs "strong binding" arrows (red) are based on affinity measurements of Buckley et al (2014) and Wang et al (2022) (as in Fig. S7). α-cat N-terminal domains in blue, M1 in green, M2 in yellow and M3 in orange. (**B**) Schematic of α-cat-H0-FABD$^+$ protein binding actin filament under low or no tension (left) based on affinity measurements of Ishiyama et al (2018). Tension-dependent affinity change remains untested for α-cat-H0-FABD$^+$ protein, but speculated based on α-cat-ΔH0-H1-FABD$^+$ protein analysis of Wang et al (2022) (also in Fig. S7). Similar α18 monoclonal antibody and vinculin accessibility observed for both WT α-cat and α-cat-H0-FABD$^+$. Only α-cat-M^{OpenKRR} and α-cat-M^{OpenDDD} show evidence of persistent vinculin and ppMLC recruitment (Fig. 3, 9 and Fig. S5, S6). Activating and inhibitory arrows show consequences of "force-desensitized" α-cat unfolding mutants for epithelial properties: Static epithelial sheet strength is greatest in the α-cat-H0-FABD$^+$ mutant, with α-cat-M-domain salt-bridge mutants showing intermediate-to-wild-type levels of cohesion despite increased recruitment of vinculin (and likely other) partners; dynamic epithelial sheet migration is most strongly perturbed in an M-domain unfolding mutant. Created with BioRender.

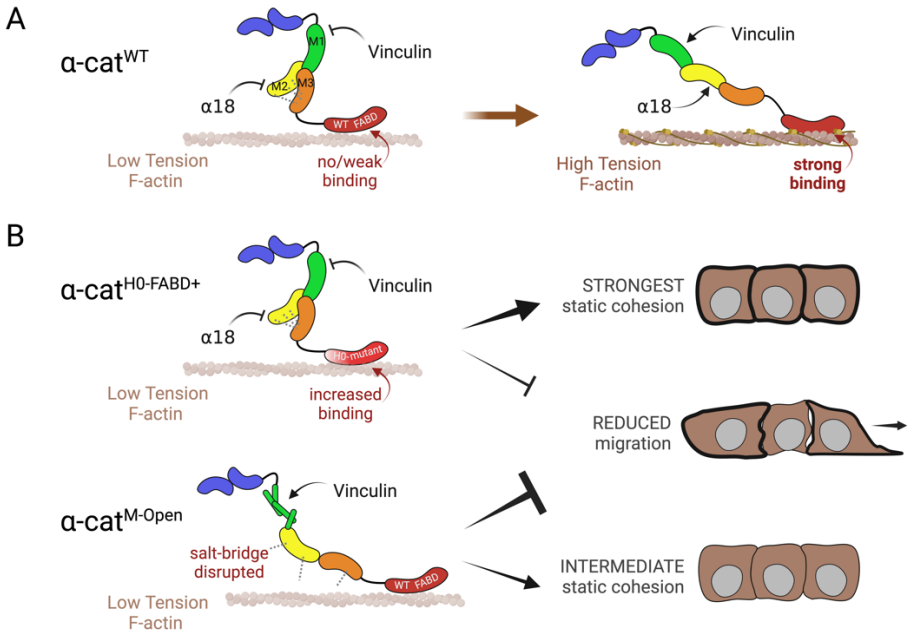

REFERENCES

Angelini, T.E., E. Hannezo, X. Trepat, J.J. Fredberg, and D.A. Weitz. 2010. Cell migration driven by cooperative substrate deformation patterns. *Phys Rev Lett*. 104:168104.

Arbore, C., M. Sergides, L. Gardini, G. Bianchi, A.V. Kashchuk, I. Pertici, P. Bianco, F.S. Pavone, and M. Capitanio. 2022. alpha-catenin switches between a slip and an asymmetric catch bond with F-actin to cooperatively regulate cell junction fluidity. *Nat Commun*. 13:1146.

Armon, S., M.S. Bull, A. Aranda-Diaz, and M. Prakash. 2018. Ultrafast epithelial contractions provide insights into contraction speed limits and tissue integrity. *Proc Natl Acad Sci U S A*. 115:E10333-E10341.

Bakolitsa, C., D.M. Cohen, L.A. Bankston, A.A. Bobkov, G.W. Cadwell, L. Jennings, D.R. Critchley, S.W. Craig, and R.C. Liddington. 2004. Structural basis for vinculin activation at sites of cell adhesion. *Nature*. 430:583-586.

Bakolitsa, C., J.M. de Pereda, C.R. Bagshaw, D.R. Critchley, and R.C. Liddington. 1999. Crystal structure of the vinculin tail suggests a pathway for activation. *Cell*. 99:603-613.

Barrick, S., J. Li, X. Kong, A. Ray, E. Tajkhorshid, and D. Leckband. 2018. Salt bridges gate alpha-catenin activation at intercellular junctions. *Mol Biol Cell*. 29:111-122.

Borgon, R.A., C. Vonrhein, G. Bricogne, P.R. Bois, and T. Izard. 2004. Crystal structure of human vinculin. *Structure*. 12:1189-1197.

Buckley, C.D., J. Tan, K.L. Anderson, D. Hanein, N. Volkmann, W.I. Weis, W.J. Nelson, and A.R. Dunn. 2014. Cell adhesion. The minimal cadherin-catenin complex binds to actin filaments under force. *Science*. 346:1254211.

Cho, Y., D. Haraguchi, K. Shigetomi, K. Matsuzawa, S. Uchida, and J. Ikenouchi. 2022. Tricellulin secures the epithelial barrier at tricellular junctions by interacting with actomyosin. *J Cell Biol*. 221.

Daugherty, R.L., L. Serebryannyy, A. Yemelyanov, A.S. Flozak, H.J. Yu, S.T. Kosak, P. De Lanerolle, and C.J. Gottardi. 2014. α-Catenin is an inhibitor of transcription. *Proceedings of the National Academy of Sciences of the United States of America*. 111:5260-5265.

Donker, L., R. Houtekamer, M. Vliem, F. Sipieter, H. Canever, M. Gomez-Gonzalez, M. Bosch-Padros, W.J. Pannekoek, X. Trepat, N. Borghi, and M. Gloerich. 2022. A mechanical G2 checkpoint controls epithelial cell division through E-cadherin-mediated regulation of Wee1-Cdk1. *Cell Rep*. 41:111475.

Green, K.J., S. Getsios, S. Troyanovsky, and L.M. Godsel. 2010. Intercellular junction assembly, dynamics, and homeostasis. *Cold Spring Harb Perspect Biol*. 2:a000125.

Harris, T.J., and U. Tepass. 2010. Adherens junctions: from molecules to morphogenesis. *Nat Rev Mol Cell Biol*. 11:502-514.

Hildebrand, J.D. 2005. Shroom regulates epithelial cell shape via the apical positioning of an actomyosin network. *Journal of cell science*. 118:5191-5203.

Hirano, Y., Y. Amano, S. Yonemura, and T. Hakoshima. 2018. The force-sensing device region of alpha-catenin is an intrinsically disordered segment in the absence of intramolecular stabilization of the autoinhibitory form. *Genes Cells*. 23:370-385.

Huang, D.L., N.A. Bax, C.D. Buckley, W.I. Weis, and A.R. Dunn. 2017. Vinculin forms a directionally asymmetric catch bond with F-actin. *Science*. 357:703-706.

Ichii, T., and M. Takeichi. 2007. p120-catenin regulates microtubule dynamics and cell migration in a cadherin-independent manner. *Genes Cells*. 12:827-839.

Ishiyama, N., S.H. Lee, S. Liu, G.Y. Li, M.J. Smith, L.F. Reichardt, and M. Ikura. 2010. Dynamic and static interactions between p120 catenin and E-cadherin regulate the stability of cell-cell adhesion. *Cell*. 141:117-128.

869 Ishiyama, N., R. Sarpal, M.N. Wood, S.K. Barrick, T. Nishikawa, H. Hayashi, A.B. Kobb, A.S.
870 Flozak, A. Yemelyanov, R. Fernandez-Gonzalez, S. Yonemura, D.E. Leckband, C.J.
871 Gottardi, U. Tepass, and M. Ikura. 2018. Force-dependent allostery of the alpha-catenin
872 actin-binding domain controls adherens junction dynamics and functions. *Nat Commun*.
873 9:5121.
874 Ishiyama, N., N. Tanaka, K. Abe, Y.J. Yang, Y.M. Abbas, M. Umitsu, B. Nagar, S.A. Bueler, J.L.
875 Rubinstein, M. Takeichi, and M. Ikura. 2013. An autoinhibited structure of alpha-catenin
876 and its implications for vinculin recruitment to adherens junctions. *J Biol Chem*.
877 288:15913-15925.
878 Kim, T.J., S. Zheng, J. Sun, I. Muhamed, J. Wu, L. Lei, X. Kong, D.E. Leckband, and Y. Wang.
879 2015. Dynamic visualization of alpha-catenin reveals rapid, reversible conformation
880 switching between tension states. *Curr Biol*. 25:218-224.
881 Labun, K., T.G. Montague, M. Krause, Y.N. Torres Cleuren, H. Tjeldnes, and E. Valen. 2019.
882 CHOPCHOP v3: expanding the CRISPR web toolbox beyond genome editing. *Nucleic*
883 *Acids Res*. 47:W171-W174.
884 Leckband, D.E., and J. de Rooij. 2014. Cadherin adhesion and mechanotransduction. *Annual*
885 *review of cell and developmental biology*. 30:291-315.
886 Li, J., J. Newhall, N. Ishiyama, C. Gottardi, M. Ikura, D.E. Leckband, and E. Tajkhorshid. 2015.
887 Structural Determinants of the Mechanical Stability of alpha-Catenin. *J Biol Chem*.
888 290:18890-18903.
889 Liberzon, A., T. Käufer, A. Bauer, P. Vennemann, and E. Zimmer. 2021. Openpiv/openpiv-
890 python: Openpiv-python V0.23.4. *In* Zenodo.
891 Maki, K., S.W. Han, Y. Hirano, S. Yonemura, T. Hakoshima, and T. Adachi. 2018. Real-time
892 TIRF observation of vinculin recruitment to stretched alpha-catenin by AFM. *Sci Rep*.
893 8:1575.
894 Matsuzawa, K., T. Himoto, Y. Mochizuki, and J. Ikenouchi. 2018. alpha-Catenin Controls the
895 Anisotropy of Force Distribution at Cell-Cell Junctions during Collective Cell Migration.
896 *Cell Rep*. 23:3447-3456.
897 McEwen, A.E., M.T. Maher, R. Mo, and C.J. Gottardi. 2014. E-cadherin phosphorylation occurs
898 during its biosynthesis to promote its cell surface stability and adhesion. *Mol Biol Cell*.
899 25:2365-2374.
900 Mei, L., S. Espinosa de Los Reyes, M.J. Reynolds, R. Leicher, S. Liu, and G.M. Alushin. 2020.
901 Molecular mechanism for direct actin force-sensing by alpha-catenin. *Elife*. 9.
902 Monster, J.L., L. Donker, M.J. Vliem, Z. Win, H.K. Matthews, J.S. Cheah, S. Yamada, J. de
903 Rooij, B. Baum, and M. Gloerich. 2021. An asymmetric junctional mechanoresponse
904 coordinates mitotic rounding with epithelial integrity. *J Cell Biol*. 220.
905 Nagafuchi, A., S. Ishihara, and S. Tsukita. 1994. The roles of catenins in the cadherin-mediated
906 cell adhesion: functional analysis of E-cadherin-alpha catenin fusion molecules. *J Cell*
907 *Biol*. 127:235-245.
908 Nishimura, R., K. Kato, M. Saida, Y. Kamei, M. Takeda, H. Miyoshi, Y. Yamagata, Y. Amano,
909 and S. Yonemura. 2022. Appropriate tension sensitivity of alpha-catenin ensures
910 rounding morphogenesis of epithelial spheroids. *Cell Struct Funct*. 47:55-73.
911 Noordstra, I., M.D. Hermoso, L. Schimmel, A. Bonfim-Melo, D. Currin-Ross, C.N. Duong, J.M.
912 Kalappurakkal, R.G. Morris, D. Vestweber, S. Mayor, E. Gordon, P. Roca-Cusachs, and
913 A.S. Yap. 2023. An E-cadherin-actin clutch translates the mechanical force of cortical
914 flow for cell-cell contact to inhibit epithelial cell locomotion. *Dev Cell*. 58:1748-1763
915 e1746.
916 Pang, S.M., S. Le, A.V. Kwiatkowski, and J. Yan. 2019. Mechanical stability of alphaT-catenin
917 and its activation by force for vinculin binding. *Mol Biol Cell*. 30:1930-1937.

Pokutta, S., and W.I. Weis. 2000. Structure of the dimerization and beta-catenin-binding region of alpha-catenin. *Mol Cell*. 5:533-543.

Rangarajan, E.S., and T. Izard. 2012. The cytoskeletal protein alpha-catenin unfurls upon binding to vinculin. *J Biol Chem*. 287:18492-18499.

Rangarajan, E.S., and T. Izard. 2013. Dimer asymmetry defines alpha-catenin interactions. *Nat Struct Mol Biol*. 20:188-193.

Sakakibara, S., K. Mizutani, A. Sugiura, A. Sakane, T. Sasaki, S. Yonemura, and Y. Takai. 2020. Afadin regulates actomyosin organization through alphaE-catenin at adherens junctions. *J Cell Biol*. 219.

Saksens, N.T., M.P. Krebs, F.E. Schoenmaker-Koller, W. Hicks, M. Yu, L. Shi, L. Rowe, G.B. Collin, J.R. Charette, S.J. Letteboer, K. Neveling, T.W. van Moorsel, S. Abu-Ltaif, E. De Baere, S. Walraedt, S. Banfi, F. Simonelli, F.P. Cremers, C.J. Boon, R. Roepman, B.P. Leroy, N.S. Peachey, C.B. Hoyng, P.M. Nishina, and A.I. den Hollander. 2016. Mutations in CTNNA1 cause butterfly-shaped pigment dystrophy and perturbed retinal pigment epithelium integrity. *Nat Genet*. 48:144-151.

Sarpal, R., M. Pellikka, R.R. Patel, F.Y. Hui, D. Godt, and U. Tepass. 2012. Mutational analysis supports a core role for Drosophila alpha-catenin in adherens junction function. *Journal of cell science*. 125:233-245.

Sarpal, R., V. Yan, L. Kazakova, L. Sheppard, J.C. Yu, R. Fernandez-Gonzalez, and U. Tepass. 2019. Role of alpha-Catenin and its mechanosensing properties in regulating Hippo/YAP-dependent tissue growth. *PLoS Genet*. 15:e1008454.

Seddiki, R., G. Narayana, P.O. Strale, H.E. Balcioglu, G. Peyret, M. Yao, A.P. Le, C. Teck Lim, J. Yan, B. Ladoux, and R.M. Mege. 2018. Force-dependent binding of vinculin to alpha-catenin regulates cell-cell contact stability and collective cell behavior. *Mol Biol Cell*. 29:380-388.

Sheppard, L., D.G. Green, G. Lerchbaumer, K.E. Rothenberg, R. Fernandez-Gonzalez, and U. Tepass. 2023. The alpha-Catenin mechanosensing M region is required for cell adhesion during tissue morphogenesis. *J Cell Biol*. 222.

Tanner, A., H.W. Chan, J.S. Pulido, G. Arno, R. Ba-Abbad, N. Jurkute, A.G. Robson, C.A. Egan, H. Knight, A. Calcagni, R.L. Taylor, E. Lenassi, G.C. Black, A.T. Moore, M. Michaelides, A.R. Webster, and O.A. Mahroo. 2021. Clinical and Genetic Findings in CTNNA1-Associated Macular Pattern Dystrophy. *Ophthalmology*. 128:952-955.

Terekhova, K., S. Pokutta, Y.S. Kee, J. Li, E. Tajkhorshid, G. Fuller, A.R. Dunn, and W.I. Weis. 2019. Binding partner- and force-promoted changes in alphaE-catenin conformation probed by native cysteine labeling. *Sci Rep*. 9:15375.

Thomas, W.A., C. Boscher, Y.S. Chu, D. Cuvelier, C. Martinez-Rico, R. Seddiki, J. Heysch, B. Ladoux, J.P. Thiery, R.M. Mege, and S. Dufour. 2013. alpha-Catenin and vinculin cooperate to promote high E-cadherin-based adhesion strength. *J Biol Chem*. 288:4957-4969.

Tuladhar, R., Y. Yeu, J. Tyler Piazza, Z. Tan, J. Rene Clemenceau, X. Wu, Q. Barrett, J. Herbert, D.H. Mathews, J. Kim, T. Hyun Hwang, and L. Lum. 2019. CRISPR-Cas9-based mutagenesis frequently provokes on-target mRNA misregulation. *Nat Commun*. 10:4056.

Twiss, F., Q. Le Duc, S. Van Der Horst, H. Tabdili, G. Van Der Krogt, N. Wang, H. Rehmann, S. Huveneers, D.E. Leckband, and J. De Rooij. 2012. Vinculin-dependent Cadherin mechanosensing regulates efficient epithelial barrier formation. *Biol Open*. 1:1128-1140.

van den Goor, L., and A.L. Miller. 2022. Closing the gap: Tricellulin/alpha-catenin interaction maintains epithelial integrity at vertices. *J Cell Biol*. 221.

Wang, A., A.R. Dunn, and W.I. Weis. 2022. Mechanism of the cadherin-catenin F-actin catch bond interaction. *Elife*. 11.

968 Wood, M.N., N. Ishiyama, I. Singaram, C.M. Chung, A.S. Flozak, A. Yemelyanov, M. Ikura, W.
969 Cho, and C.J. Gottardi. 2017. alpha-Catenin homodimers are recruited to
970 phosphoinositide-activated membranes to promote adhesion. *J Cell Biol*. 216:3767-
971 3783.
972 Xu, X.P., S. Pokutta, M. Torres, M.F. Swift, D. Hanein, N. Volkmann, and W.I. Weis. 2020.
973 Structural basis of alphaE-catenin-F-actin catch bond behavior. *Elife*. 9.
974 Yao, M., W. Qiu, R. Liu, A.K. Efremov, P. Cong, R. Seddiki, M. Payre, C.T. Lim, B. Ladoux,
975 R.M. Mege, and J. Yan. 2014. Force-dependent conformational switch of alpha-catenin
976 controls vinculin binding. *Nat Commun*. 5:4525.
977 Yonemura, S., Y. Wada, T. Watanabe, A. Nagafuchi, and M. Shibata. 2010. alpha-Catenin as a
978 tension transducer that induces adherens junction development. *Nature cell biology*.
979 12:533-542.
980 Zacharias, D.A. 2002. Sticky caveats in an otherwise glowing report: oligomerizing fluorescent
981 proteins and their use in cell biology. *Sci STKE*. 2002:pe23.

982